Journal of the Meteorological Society of Japan

# EARLY ONLINE RELEASE



The DOI for this manuscript is

DOI:10.2151/jmsj.2020-012

J-STAGE Advance published date: November 30th, 2019

# Statistical Characteristics of Pre-Summer Rainfall over South China and Associated Synoptic Conditions

Zhenghui Li[1,2], Yali Luo[1,3*], Yu Du[4], and Johnny C. L. Chan[5]

*[1] State Key Laboratory of Severe Weather, Chinese Academy of Meteorological Sciences, Beijing, China*
*[2] University of Chinese Academy of Sciences, Beijing, China*
*[3] Collaborative Innovation Center on Forecast and Evaluation of Meteorological Disasters, Nanjing University of Information Science and Technology, Nanjing, China*
*[4] School of Atmospheric Sciences, and Guangdong Province Key Laboratory for Climate Change and Natural Disaster Studies, Sun Yat-sen University, Guangzhou, China, and Southern Marine Science and Engineering Guangdong Laboratory (Zhuhai), Zhuhai, China*
*[5] Guy Carpenter Asia-Pacific Climate Impact Centre, School of Energy and Environment, City University of Hong Kong, Hong Kong SAR, China*

*Journal of the Meteorological Society of Japan*

Submitted December 11, 2018
Revised 6 May, 2019
2nd revised 1 July, 2019
Revised 5 Sept., 2019
Revised 23 October, 2019

* Corresponding author: Dr. Yali Luo, State Key Laboratory of Severe Weather, Chinese Academy of Meteorological Sciences, Beijing 100081, China
E-mail: ylluo@cma.gov.cn; yali.luo@qq.com
Tel: +86-10-68408418 Fax: +86-10-62175931

## Abstract

Climatological characteristics of pre-summer (April-to-June) rainfall over Southern China (SC) and associated synoptic conditions are examined using 1980-2017 hourly rainfall observations and reanalysis data. The rainfall amount, frequency, and intensity show pronounced regional variations and substantial changes between pre- and post-monsoon-onset periods. Owing to more favorable thermodynamic conditions after monsoon onset over South China Sea (SCS), rainfall intensifies generally over entire SC irrespective of the rainfall-event durations. Increased magnitudes of rainfall amount in longer-duration (>6 h) events are found over a designated west-inland region (west of 111°E), which are partially attributed to enhanced dynamic instability. In addition, rainfall events occur more frequently over the west-inland region, as well as coastal regions west side of 118°E, but less over a designated east-inland region. The inland-region rainfall is closely linked to dynamic lifting driven by subtropical synoptic systems (low pressure and an associated front or shearline). The westward extension of the western North Pacific high and the eastward extension/movement of the front or shearline, interacting with the intra-period intensification of the southwesterly monsoonal flows, play important roles in providing high-$\theta_e$ (equivalent potential temperature) air to the west- and east-inland regions, respectively. The warm-sector, coastal rainfall is closely related to the deceleration of the southerly boundary layer (BL) jet (BLJ) over the northern SCS and associated convergence of BL high-$\theta_e$ air near the coast. Meanwhile the southwesterly synoptic-system-related low-level jet in the lower-to-middle troposphere to the south of the inland cold front can contribute to the coastal rainfall occurrence by providing divergence above the BL convergence near the coast. The BLJ often simultaneously strengthens with the lower-troposphere horizontal winds, suggesting a close association between the BLJ and the synoptic systems. The quantitative statistics provided in this study complement previous case studies or qualitative results and thus advance understanding about pre-summer rainfall over SC.

**Keywords:** pre-summer rainfall events; monsoon onset; synoptic analysis; low-level jets; warm-sector rainfall

## 1. Introduction

South China (SC) generally refers to the region south of about 28°N and east of the Yungui Plateau (Fig. 1). Located in the East Asian monsoon region, SC is featured with a long rainy season from April to early October (Ramage 1952). Owing to the frequent occurrence of heavy rainfall at hourly to longer time scales during the rainy season (Zheng et al. 2016), SC is exposed to high-risk of flash flooding and inundation (Hallegatte et al. 2013). In accordance with the subseasonal migration of the East Asian summer monsoon (EASM) circulation and rainfall (Ding 1994; Ding and Chan 2005), the rainy season in SC can be divided into the early and late periods with a demarcation between the two being the end of June (Yuan et al. 2010). The early period (April to June) is the pre-summer rainy season, occurring during the early stage of the EASM and accounting for about a half of the annual rainfall amount (Luo 2017). Hence, improved understanding of regional variations in characteristics of the pre-summer rainfall over SC and the associated synoptic conditions is expected to advance rainfall forecast skill, which is of importance to the local society.

The pre-summer rainy season in SC covers two subperiods that are referred to as the *pre-* and *post-monsoon-onset periods*, respectively (e.g., Jiang et al. 2017; Chen and Luo 2018). After the onset of the South China Sea (SCS) monsoon in mid-to-late May (Xie et al. 1998; Luo et al. 2013), heavy rainfall events during the pre-summer rainy season tend to occur more frequently (Ding and Chan 2005) with notable changes in the paths and sources of moisture supplied to SC (Chen and Luo 2018). Quantitative comparisons of statistical characteristics of the pre-summer rainfall over SC between the pre- and post-monsoon-onset periods using multiple satellite products (Xu et al. 2009; Luo et al. 2013) suggest an increase in the domain-averaged rainfall accumulation and generally enhanced convective intensity after the SCS monsoon onset. However, extremely heavy rainfall exceeding 500 mm day$^{-1}$ or 180 mm h$^{-1}$ is also observed over SC even before the onset of the SCS monsoon (e.g., Wang et al. 2014; Huang et al. 2019).

The major large-scale weather systems governing pre-summer rainfall over SC include middle-high-latitude troughs and ridges, south Asia high pressure systems, SCS monsoon surges, and subtropical highs centered over the Western Pacific Ocean (Ding 1994). It has long been known that pre-summer rainfall over SC often occurs in the warm sector of a surface baroclinic wave cyclone a few hundred kilometers away from the cyclone front (Huang et al. 1986). The frontal rainfall and warm-sector rainfall may occur simultaneously in the form of dual rain belts or as a single rain belt over SC. Recent studies revealed that the warm-sector rainfall is associated with boundary layer (BL) flows of tropical origins (Luo et al. 2017), surface heating and local topographic lifting (Jiang et al. 2017), mesoscale cold pools (Wu and Luo 2016), land-sea-breeze fronts (Chen et al. 2017), terrain effects (Wang et al. 2014; Tu et al. 2014), and urban heat island effects interacting with sea breezes (Wu et al.

2019). Heavy-rainfall case studies showed that the dual rain belts simultaneously observed over inland and coastal SC can be closely related to the coupling of a BL jet (BLJ) and a synoptic-system-related low-level jet (SLLJ) (Du and Chen 2018; 2019). However, a systematic analysis is still lacking related to synoptic conditions for pre-summer rainfall over SC. In particular, few studies have made a comparison of the synoptic conditions among the subregions of SC during the pre-summer rainy season, or between the pre- and post-monsoon-onset periods.

This study investigates statistical characteristics of pre-summer rainfall over SC and its associated synoptic conditions with a focus on comparisons between the inland and coastal regions, as well as between the pre- and post-monsoon-onset periods. The next section describes the data and analysis methods. Section 3 compares the statistical characteristics of the rainfall events between the pre- and post-monsoon-onset periods of 1980-2017. Synoptic conditions on long-duration rainy days (definition will be given in section 2.3) over the inland SC regions are discussed in section 4. For the long-duration rainy days over the coastal region that occur on their own or simultaneously with the long-duration rainy days over the inland region, synoptic conditions are presented in section 5 with emphasis on the LLJs. Summary and conclusions are provided in section 6.

## 2. Data and methods

### *2.1 Determination of the SCS monsoon onset*

In this study, the onset time of the SCS summer monsoon is determined following the National Climate Center of China Meteorological Administration (CMA) (http://cmdp.ncc-cma.net/Monitoring/monsoon.php). It is the first pentad when the 850-hPa zonal wind steadily (for two pentads with break at most one pentad, or last for more than two pentads continuously) changes from easterly to westerly and the 850-hPa equivalent potential temperature ($\theta_e$) is $\geqslant$ 340 K averaged over the SCS area (10°–20°N, 110°–120°E). The *pre-monsoon-onset period* is defined as that from 1 April to the earlier-half of the onset pentad, while the *post-monsoon-onset period* consists of the days from the later-half of the onset pentad to 30 June. Using the European Centre for Medium-Range Weather Forecasts (ECMWF) Interim Re-Analysis data set (ERA-Interim; Dee et al. 2011; https://www.ecmwf.int/en/forecasts/datasets/archive-datasets/reanalysis-datasets/era-interim) with a horizontal resolution of 0.25° × 0.25°, the monsoon onset pentad is determined for each year of 1980-2017. The results suggest that the SCS monsoon onset occurs mostly in mid-to-late May, in agreement with previous studies (Xie et al. 1998; Luo et al. 2013). The earliest onset in this study occurs in the 24$^{th}$ pentad (26-30 April; 2012) and latest in the 32$^{th}$ pentad (6-10 June; 1987, 1989, 1991, 2004). The 1980-2017 pre- and post-monsoon-onset periods, respectively, are 49.6 and 41.4 days per year on the average.

*2.2 Definition of the rainfall events*

The quality-controlled long-term, gauge-based hourly rainfall dataset from the National Meteorological Information Center (NMIC) of CMA is used to investigate the statistical characteristics of the pre-summer rainfall. A quality-control procedure has been applied to the dataset by NMIC, consisting of a climatological limit value test, a station extreme value test, an internal consistency test, and a comparison with manually checked daily rainfall data. This dataset has been extensively used to investigate the characteristics of sub-daily rainfall over China (e.g., Yu et al. 2007, 2013; Li et al. 2008, 2013; Luo et al. 2016). The present study utilizes 303 meteorological stations in SC (Fig. 1) that have continuous records from 1980 to 2017.

Three subregions in SC are selected with distinct topographical features and pre-summer rainfall properties, such as diurnal variations (Jiang et al. 2017) and convective intensity (Xu et al. 2009; Luo et al. 2013). The subregions are the *west-inland*, *east-inland*, and *coastal* regions (Fig. 1). The west-inland region is located to the east of the Yungui Plateau, covering most Guangxi (GX) province and southeast Guizhou province. The east-inland is a hilly region including north Guangdong (GD), southwest Fujian (FJ), south Jiangxi, and southeast Hunan. The coastal region mostly includes coastal GD and is relatively flat with small, scattered hills.

A "rainfall event" is defined following Yu et al. (2007), specifically, a spell that has measurable rainfall ($\geqslant$ 0.1 mm $h^{-1}$) without any or at most a one-hour interruption (Li et al. 2013; Yu et al. 2013). After a rainfall event begins, if its interruption lasts for two hours, the rainfall that follows belongs to a new rainfall event. The duration of a rainfall event is the length of time between the beginning and the end of the event. According to their durations, rainfall events are classified into the *short*- (1-6 h), *moderate*- (7-12 h), and *long-duration* (>12 h) categories. For each rainfall-event type, accumulated rainfall amount, occurrence frequency, and hourly rainfall intensity are comparatively analyzed for the pre- and post-monsoon-onset periods.

*2.3 Analysis of the synoptic conditions*

Occurrence of the long-duration rainfall events simultaneously at a considerable fraction of stations over a region is expected to be associated with prominent synoptic-scale forcing (Holton 2004); while synoptic forcing is often weak for shorter-duration, local-scale rainfall in a region (Guo et al. 2017). In this study *a long-duration rainy day* of a subregion is defined as a day (1200-1200 UTC) when at least 15% stations in the subregion having a long-duration rainfall event. If long-duration rainfall at a station spans 12 UTC, it belongs to both days before and after for that station. By such a definition, rainfall events with short-, moderate-, and long-durations may occur simultaneously over the subregion on a long-duration rainy day. Our analysis results indicate that the west-inland region has 246 and 303 long-duration rainy days accounting for 13% and 19% of the 1980-2017 pre- and post-monsoon-onset periods, respectively. The numbers (percentages) of long-duration rainy days are 514 (27%) and 338 (21%) for the east-inland region and 316 (17%) and 273 (17%) for the coastal region. Concurrence of the long-duration rainy days over the coastal subregion and the east-inland subregion is often observed, sometimes over the two inland subregions, and occasionally over the three subregions (Fig. 2). These statistics further supplement those of previous case studies that found existence of dual rain belts over coastal and inland SC during the pre-summer rainy season (Huang et al. 1986; Ding 1994; Du and Chen 2018; Liu et al. 2018).

To examine the synoptic-scale circulation and thermodynamic conditions on the long-duration rainy days over the selected subregions, composite and anomalous fields of relevant variables such as horizontal and vertical winds, vertical vorticity, potential vorticity, $\theta_e$, and precipitable water (PW) are analyzed using ERA-interim data. The composite fields of each variable are obtained by averaging all 6-hourly fields of the variable on the long-duration rainy days for the selected subregion(s). The anomalous fields are calculated as composite minus the corresponding 1980-2017 climatology (i.e., average over all the 6-hourly re-analysis data) during the pre- and post-monsoon-onset periods, respectively.

The presence and structure of LLJs are analyzed using ERA-interim data, largely following the methods adopted by Du et al. (2014) to reveal their possible relation with the pre-summer rainfall over the SC coast. The following criteria are used to identify LLJs: 1) the maximum wind speed in the lowest 13 layers (below approximately 4 km) is more than 10 m $s^{-1}$ with wind direction between 90-270 degrees (southwesterly-to-southeasterly) and 2) the wind speed must decrease by at least 3 m $s^{-1}$ from the height of the wind maximum to the wind minimum above that level. These criteria are similar to those adopted by Du et al. (2012, 2014), Pham et al. (2008), and Whiteman et al. (1997). The height of the LLJs is defined as the height of the horizontal wind speed maxima where the LLJs occur. Then the LLJs are classified into BLJs (occurring approximately below the 1-km level) and SLLJs (occurring approximately between the 1-km and 4-km levels). It is possible for a BLJ and a SLLJ to occur at the same time with a double peak in the vertical profile of wind speed, although this does not occur very often. When the double peak occurs, both peaks are counted. Furthermore, the SLLJs (BLJs) with grids less than 25% (10%) in the region of (110-118$^{o}$E, 18-27$^{o}$N) (dashed box in Fig. 1) are removed.

## 3. Amount, occurrence frequency, and intensity of rainfall events

### *3.1 Domain-average statistics*

The SC domain-averaged rainfall statistics in 1980-2017 are shown in Table 1. Compared to the pre-monsoon-onset period, the rainfall amount accumulated during the post-monsoon-onset period increases by 8.3% despite of its shorter span (41.4 vs. 49.6 days per year) and smaller number of rainfall events (31.1 vs. 35.5 per station per year). The daily-averaged rainfall amount shows a substantial increase (30.4%) after the SCS monsoon onset, while the occurrence frequency of the rainfall events increases slightly (4.2%) and their hourly rainfall intensity is enhanced by 26.5%. These results are mainly attributed to more favorable thermodynamic conditions for rainfall production over SC, i.e., the higher convective available potential energy (CAPE) and larger amount of PW (Luo et al. 2013). The average duration of rainfall events decreases slightly (from 4.3 to 4.2 h) due to a larger number of short-duration rainfall events in the post-monsoon-onset period (Fig. 3b).

Figure 3 shows statistics of rainfall amount, occurrence frequency, and average rainfall intensity for the three rainfall-event types classified according to their duration. The short-duration type produces a larger amount of rainfall accumulation over SC than the other two types with longer durations (Fig. 3a), because of its substantially larger population (roughly 4~5 times greater than the moderate-duration event) in each period (Fig. 3b). Compared to the pre-monsoon-onset period, all three types have larger rainfall amounts during the post-monsoon-onset period (Fig. 3a). The largest increase in rainfall amount among the three types is observed in the long-duration type, with its median and maximal values among the stations increasing about 61% and 58%, respectively. Increasing ratios of the moderate-duration type are the lowest (10% and 26%) among the three rainfall-event types, with those of the short-duration type in between (19% and 30%). After the SCS monsoon onset, the occurrence frequency increases for the short-duration type, but remains about the same for the longer-duration types (Fig. 3b), while the average hourly rainfall intensity of all types is strengthened, especially the long-duration type (Fig. 3c).

In short, after the SCS monsoon onset, all the three rainfall-event types over SC possess enhanced hourly rainfall intensity particularly for the long-duration type. Occurrence frequency of the short-duration rainfall events increases, which can be attributed to more frequent occurrence of thermally driven local-scale rainfall occurring in the afternoon (Dai et al. 1999; Luo et al. 2016). These changes can also be attributed to the more favorable thermodynamic and moisture conditions over SC.

### *3.2 Regional variations*

The range and distribution of rainfall amounts and intensities at individual stations over SC are presented in Fig. 4. Histograms and cumulative distribution functions (CDFs) of rainfall amount during the pre- and post-monsoon-onset periods, respectively, are shown in Figs. 4a and 4b. An examination of the rainfall amount histograms suggests that the fraction of stations with light rainfall (< 5 mm day$^{-1}$) decreases substantially from about 32.7% to 1.3%, whilst that with heavier rainfall (> 10 mm day$^{-1}$) increases from 1.3% to 11.2% after the SCS monsoon onset. Spatial distribution of the rainfall amount during the pre-monsoon-onset period shows three areas of higher rainfall amounts (about 10 mm day$^{-1}$) in central GD, coastal southwest GD, and northeast GX (Fig. 4c). After the SCS monsoon onset, central and costal GD and northeast GX have higher rainfall amounts (about 12.5 mm day$^{-1}$) relative to other places of SC (Fig. 4d). The differences (post- minus pre-monsoon-onset period) in the rainfall amount (Fig. 4e) are positive at most stations except for some stations over the east-inland region. The largest increase (> 5 mm day$^{-1}$) in the rainfall amount is observed in the west-inland and coastal regions.

The histograms of occurrence frequency of the rainfall events suggest that the frequency at the stations ranges from 0.2 to 1.1 event day$^{-1}$ during both periods (Figs. 5a, 5b). The value exceeding 1.0 is due to one station has a larger number of rainfall events than the number of days during each period. The stations with low rainfall-event frequency (< 0.6 event day$^{-1}$) account for 19% of the population (Fig. 5a) and are located mostly in the west-inland and coastal regions in the pre-monsoon-onset period (Fig. 5c). In contrast, such stations only account for 6% of the population (Fig. 5b) and are scattered over north and southwest of SC in the post-monsoon-onset period (Fig. 5d). Spatial distribution of the difference in the occurrence frequency shows an overall decrease over the east-inland region and a contrasting increase over the west-inland and coastal regions after the monsoon onset (Fig. 5e). The former is contributed by the less occurrence of the three types of rainfall events over the northern portion of the east-inland region (approximately north of 25°N), while the latter mainly by the greater occurrence of the short-duration rainfall events (Fig. 6). The relatively more frequent rainfall events over the northern portion of the east-inland region before the SCS monsoon onset is closely related to the persistent rainfall south of the Yangtze River (112°E-120°E, 25°N-30°N) in spring (mid-March to early May) (Tian and Yasunari 1998; Zhao et al. 2008; Huang et al. 2015; Luo et al. 2016). Formation of such persistent rainfall in spring is attributed to the moisture convergence and upward motion as a result from both the retarding and deflecting effects of the TP on the westerlies (Wu et al. 2007) and the thermal contrast between western China and the subtropical western Pacific (P. Zhao et al. 2007).

As is the case for the rainfall amount CDFs (Figs. 4a, 4b), the rainfall intensity CDFs also shift toward the larger values in the post-monsoon-onset period (Figs. 7a, 7b), reflecting a general enhancement of rainfall intensity at the stations and consistent with Fig. 3c. The spatial distributions present a strong dependence of rainfall strength on the latitude (i.e., more intense at lower latitudes) during both periods (Figs. 7c, 7d). The areas of strong rainfall intensity in GD and GX largely correspond to frequent occurrence of convective precipitation features observed by the TRMM precipitation radar (PR; Kummerow et al. 1998) shown in Luo et al. (2013). In contrast, the weaker rainfall intensity over northern SC has high (low) occurrence frequency of non-convective (convective) precipitation features observed by the TRMM PR (Luo et al. 2013). The differences in rainfall intensity between the post- and pre-monsoon-onset periods (post- minus pre-monsoon-onset period) are positive at almost all the stations, with relatively larger increases in the west-inland region (Fig. 7e) mainly contributed by the intensification of longer-duration events (not shown).

In summary, after the SCS monsoon onset, hourly rainfall intensities of the rainfall events are generally strengthened over SC, especially the longer-duration (>6 h) events over the west-inland region. All the three types of rainfall events, particularly the short-duration events, occur more frequently in the west-inland and coastal regions, but the rainfall events occur less frequently over the northern portion of the east-inland region during the post-monsoon-onset period. As a result, a substantial increase in accumulated rainfall amounts is observed in the west-inland and coastal regions during the post-monsoon-onset period, whilst the rainfall amounts in the east-inland region during the two periods are nearly comparable.

## 4. Synoptic background on the inland long-duration rainy days

During the pre-monsoon-onset period of the 1980-2017, 246 and 514 long-duration rainy days (definition given in section 2.3) are found over the west- and east-inland subregions, respectively (Fig. 2). Among those days, 110 days are overlapping for the west- and east-inland regions (but not the coastal region). Similarly, 303 and 338 long-duration rainy days are found during the post-monsoon-onset period over the west- and east-inland subregions, respectively, including 88 days over both inland subregions (but not the coastal region). To better understand the thermodynamic and dynamic conditions under which the long-duration rainy events occur over the inland regions, this section presents the composite and anomalous fields on three groups of the long-duration rainy days, namely, the west-inland only (first group), both inland regions (second group), and east-inland only (third group), respectively.

### *4.1 The pre-monsoon-onset period*

Similar patterns are found in the 850 hPa composite fields on the long-duration rainy days of the pre-monsoon-onset period over the west-inland only

(88 days), both inland regions (110 days), and east-inland region only (209 days) (Figs. 8a-c). The 850 hPa geopotential height ($H_g$) field shows low pressure near the west-inland region and high pressure over the western North Pacific. A southwest-northeast-oriented shearline extends from the west-inland region toward central east China. Along the shearline a sign change in $\partial pv / \partial y$ ($pv$ is the potential vorticity) is observed (the layer of reversed $pv$ gradient reaches about 800 hPa; not shown), suggesting that the Charney-Stern instability criterion (Charney and Stern 1962) is satisfied there. Large southward gradients of $\theta_e$ and large standard deviations of meridional wind ($v$) are found in the northern portion of the inland regions, being more prominent in the west-inland region. The anomalous fields (Figs. 8d-f) show presence of northeasterly wind anomalies (being less evident for the long-duration rainfall days over west-inland only; Fig. 8d), negative $\theta_e$ anomalies to the north of the inland regions, and cyclonic vorticity anomalies around the shearline.

All these features collectively reveal a close association between the inland rainfall and subtropical synoptic systems (low pressure and associated fronts, shearlines, vortices) (Huang et al. 1986; Ding 1994). The convergence of the southerly and northerly winds results in formation of a boundary between warm moist air and cold dry air leading to upward motion within a deep moist unstable layer (S. X. Zhao et al. 2007). The cyclonic vorticity anomalies (Figs. 8d-f) can be traced back to the migratory cyclonic anomalies originated near the southeastern margin of the Tibetan Plateau a few days earlier (Li et al. 2014;

Huang et al. 2018), or are closely related to a deep trough anomaly extending from an intense cyclonic anomaly over north China, which in turn could be traced back to a midlatitude Rossby wave train passing the Tibetan Plateau (Huang et al. 2018).

Differences among the three inland-rainfall groups during the pre-monsoon-onset period are primarily detectable in the wind fields. Specifically, the first group (long-duration rainfall days over west-inland only) is characterized by strong southerly flow prevailing over the west-inland and its immediate upstream regions (Fig. 8a). The second group (long-duration rainfall days over both inland regions) exhibits strong southwesterly flow to influence the east-inland region, in addition to the southerly flow to the west (Fig. 8b). In the third group (long-duration rainfall days over east-inland only) the strong southwesterly flow possesses a larger zonal velocity component, mainly covering the east-inland and its upstream regions (Fig. 8c). Meanwhile, a moist tongue (represented by precipitable water) extends from north SCS and Gulf of Tonkin to the south boundary of the west-inland region in the first group; it broadens eastward to cover the immediate upstream portions of both west- and east-inland regions in the other two groups (Figs. 8a-c). Moreover, the western North Pacific high (WNPH) extends westward (retreats eastward) when rainfall is produced over the west-inland (east-inland) region. The easterly flows (and anomalies; Fig. 8d) prevail over northern SCS and change to southerly when approaching SC in the first and second groups, suggesting that the WNPH extends westward to persistently transport moisture (Chen and Luo 2018) and provide air masses with higher $\theta_e$ toward the west-inland region. In contrast, southwesterly flows (and anomalies; Fig. 8f) are observed over and upstream of the east-inland region in the third group, suggesting a crucial role played by intra-period intensification of the southwesterly flows on providing higher-$\theta_e$ air to the east-inland rainfall. The intensification of the southwesterly flows over the SCS may be attributed to the enhancement of the pressure gradient force between an eastward-moving low pressure from western China and a westward-moving high pressure from the western North Pacific, as found by Zhao et al. (2003) using gridded data in spring and summer of 1998 from the South China Sea Monsoon Experiment (SCSMEX; Lau et al. 2000).

*4.2 The post-monsoon-onset period*

A clear signature of the above-mentioned synoptic systems is also observed on the inland long-duration rainy days of the post-monsoon-onset period (Fig. 9). The differences among the three inland-rainfall groups during the post-monsoon-onset period can be seen in the wind and moisture fields (Figs. 9a-c). In the first group, the southwesterly flows extend from northeast of the Indochina Peninsula to western portion of SC while northern SCS is mainly influenced by weaker southerlies. In the second group, southwesterly flow prevails over a wider area to influence eastern portion of SC. In the third group, the northern SCS and east-inland SC are impacted by strong southwesterly flows. Meanwhile, the moist area extending from the SCS and Gulf of Tonkin mainly influences the west-inland region in the first group; it expands eastward to cover the east-inland region in the other two groups. These differences among the three inland-rainfall groups during the post-monsoon-onset period are at least qualitatively consistent with those during the pre-monsoon-onset period. The differences among the three groups (Figs. 8a-c, 9a-c) reflect that the southeastward- or eastward-moving low-level vortices and associated shearlines or fronts, along with the westward-expanding WNPH (not shown), sequentially or simultaneously produce rainfall over the west and east-inland SC. Such migratory synoptic systems are documented in case studies of pre-summer heavy rainfall over SC (e.g., Zhao et al. 2003; Du and Chen 2018; Zhang and Meng 2018).

Several differences in spatial patterns are apparent between the pre- and post-monsoon-onset periods (cf. Figs. 8 and 9). The southwesterly air flow strengthens significantly over SC and its upstream after the SCS monsoon onset, consistent with the increased gradients in $H_g$ field (cf. Figs. 9a-c and 8a-c). The precipitable water increases substantially over SC and north SCS, and $\theta_e$ generally becomes much higher (e.g., from 328-340 K to 344-352 K over the west-inland region). Correspondingly, the relative vorticity anomalies, which center in the west-inland region and extend toward the northeast, also have greater positive values during the post-monsoon-onset period. All these differences between the two periods collectively suggest more favorable thermodynamic conditions and dynamic instability for producing stronger rainfall intensity over the inland regions after the SCS monsoon onset.

## 5. Synoptic background on the coastal long-duration rainy days

During the 1980-2017 pre-summer rainy season, 316 and 273 long-duration rainy days are found over the coastal region of SC during the pre- and post-monsoon-onset periods, respectively (Fig. 2). Among those days, 154 and 99 days have both the coastal and east-inland regions (but not the west-inland region) as long-duration rainy days during the earlier and later periods, respectively. A concept of double LLJs (i.e., BLJ and SLLJ) and their relationship with the concurrent rain belts over inland and coastal SC has been recently proposed by Du and Chen (2018) based on a heavy-rainfall case study. Their results suggest that the inland frontal rainfall is closely related to a SLLJ with maximum wind speed at 850-700 hPa, especially for the meridional wind component; The warm-sector heavy rainfall, a few hundred kilometers away from the front, is associated with a BLJ at 925 hPa. Du and Chen (2019) further demonstrate that the nighttime BLJ over the northern SCS strengthens the convergence at ~950 hPa near the coast where the BLJ's northern terminus reaches the coastal terrain. Meanwhile, the SLLJ to the south of the inland cold front provides divergence at ~700 hPa near the SLLJ's entrance region. Such low-level convergence and mid-level divergence together produce strong mesoscale lifting for convection initiation at the coast.

This section discusses the composite synoptic background of a large ensemble of long-duration rainy days in two groups: simultaneously over both coastal and east-inland regions (but not the west-inland region; the first group), and over the coastal region only (the second group). The BL on those long-duration rainy days during the pre-monsoon-onset period (Figs. 10a, 10b) is characterized by southerly air flow from SCS to coastal SC that decelerates when approaching and crossing the SC coast. These results suggest the importance of BL southerly flow over northern SCS in producing the coastal rainfall by providing high-$\theta_e$ air to the SC coast. Differences between the two groups are more obvious to the north of SC (cf. Figs. 10a and 10b). In the former group (i.e., with long-duration rainy days simultaneously over both the coastal and east-inland regions), northeasterly flow prevails to the north of SC and penetrate to the west-inland region of SC, resulting in strong convergence over SC (red solid; Fig. 10a). Such northeasterly flow and related convergence are greatly reduced in the latter group, i.e., on the long-duration rainy days over the coastal region only (Fig. 10b).

The difference between the two groups indicates that the coastal rainfall is less associated with cold and dry air intrusion in the BL; instead it is closely related to deceleration of the southerly flow and associated convergence of BL high-$\theta_e$ air over the coast (Fig. 10b). At 850 hPa (Figs. 10c, 10d) southwesterly flow passes sequentially over the Hainan island and the SC coastal region, and further penetrates into the east-inland region with reduced speeds. The 850 hPa wind convergence at the northern terminus of the southwesterly flows is band-shaped and centered over the SC inland regions for both groups, with larger magnitudes in the first group (Figs. 10a, 10c). Over the coastal region the 850 hPa wind convergence is quite weak (Figs. 10c, 10d), in contrast to the stronger convergence in the BL (Figs. 10a, 10b).

On those long-duration rainy days during the post-monsoon-onset period, extensive southwesterly flow in the BL and lower troposphere extends from northeastern portion of Indochina Peninsula and dominates the northern SCS, Gulf of Tonkin, and SC (Fig. 11). Similar to the above-mentioned findings for the pre-monsoon-onset period, the SC coastal region is influenced by BL convergence mostly due to deceleration of the southwesterly flow (Figs. 11a,11b). Northeasterly flow is not observed in the BL and lower troposphere in the latter group (Figs. 11b,11d), although they exist several hundred kilometers away to the northwest in the former group (Figs. 11a,11c). These horizontal analysis results imply that the double LLJs (Du and Chen 2018; 2019) may occur over southern China on the coastal long-duration rainy days before and after the SCS monsoon onset, with even stronger intensities and broader expanses of the LLJs during the post- than the pre-monsoon-onset period (cf. Figs. 10 and 11).

Consistent with the horizontal analysis, vertical cross sections of winds along 112°E (the brown line in Fig. 10b) also support the possible existence of the BLJ (SLLJ) over the ocean (land) on the long-duration rainy days of the coastal region (Figs. 12a,12b,12d,12e). The entrance and exit of the LLJs are usually related to the horizontal divergence and convergence, respectively

(Hastenrath 1985), although they also depend on the jet stream configurations (Keyser and Shapiro 1986). During both pre- and post-monsoon-onset periods, BL convergence clearly exists at the exit region of the likely BLJ which is located near the coastline, with 850-700hPa weak divergence aloft at the entrance of the likely SLLJ. After the SCS monsoon onset, the BL wind speeds substantially increase, with the jet cores located farther south. A more elevated layer of convergence and upward motion is evident in the SC inland region during both periods (relatively less evident in the coastal-only cases after the monsoon-onset; Fig. 12e), which is co-located with the exit region of the SLLJ (Figs. 12a,b,d). Such a signal of double LLJs on the coastal long-duration rainy days is at least qualitatively consistent with the finding of Du et al. (2018, 2019). Such a signal is absent on the days when rainfall is not observed over the coastal region (Figs. 12c,12f). On these dry days of the coastal region, north SCS features with much weaker southerly flow (even northerly flow south of 18$^{o}$N) in the BL, while the SC coast is dominated by large-scale downward motion.

To better examine the relation between the LLJs and the SC coastal rainfall, the long-duration rainy days over both the coastal and east-inland regions are separated into two subgroups: one with (the first subgroup) and one without (the second subgroup) at least one BLJ event (definition provided in section 2.3). Their vertical cross sections are shown in Fig. 13. The above-mentioned major features of relevance to the coastal rainfall occurrence, i.e., the BL convergence coupled with divergence aloft over the coast, are observed in the first subgroup during both periods (Figs. 13a 13b) and the second subgroup before the monsoon-onset (Fig. 13c). The results indicate that the double LLJs could play important roles in the coastal rainfall, even if their wind speeds do not satisfy the criteria used to identify the BLJ- and SLLJ-events. The low-to-mid-level divergence over the coast has relatively smaller values than the BL convergence, especially on the days without the BLJ event during the post-monsoon-onset period (Fig. 13d). This indicates that the BL convergence probably plays a key role in the occurrence of the coastal rainfall, while the divergence aloft can make some contribution. Moreover, recent studies suggest that the SC coastal rainfall can be closely associated with land–sea-breeze fronts (Chen et al. 2016), coastal mountains (Wang et al. 2014), and convectively-generated cold pools (Wu and Luo 2016; Liu et al. 2018).

It is noteworthy that the lower-level (about 850 hPa) horizontal winds tend to be stronger when the BLJ events are identified on the coastal rainy days, irrespective of whether the inland rainfall is simultaneously produced (Figs. 13, 14). This analysis suggests that strength of the BLJ over northern SCS is closely related to the synoptic systems over SC (low pressure, front, shearline) and the WNPH, as noted in the case study by Du and Chen (2018). On the long-duration rainy days over both the coastal and east-inland regions, the SLLJ collides with the northerly, cold, dry airflow (Fig. 13), providing strong synoptic forcing over the inland regions. In contrast, the BLJ's northern terminus is located several hundred kilometers away from the northerly airflow, implying that local coastal processes (frictional convergence and orographic effects) rather than synoptic lifting dominate rainfall production. When only the coastal region has the long-duration rainfall events, strong synoptic forcing associated with northerly, cold, dry airflows is not found near the coast (Fig. 14). This difference in forcing mechanisms may explain the lower predictability of the pre-summer heavy rainfall over the SC coast than the inland regions (Huang and Luo 2017).

## 6. Summary and conclusions

In the present study, statistical characteristics of the rainfall events over the inland and coastal subregions of SC (Fig. 1) during the pre- and post-monsoon-onset periods of pre-summer rainy season are compared and analyzed in relation to their associated large-scale circulations. A rainfall event is defined as a period having measurable rainfall (more than 0.1 mm $h^{-1}$) without any or at most a one-hour interruption. A long-duration rainy day of a designated subregion is defined as a day when at least 15% of the stations in the subregion have a long-duration (>12 h) rainfall event. The pre-monsoon-onset period of each year covers the days from April 1 to the SCS monsoon onset, while the post-monsoon-onset period starts from the SCS monsoon onset to June 30. The principal findings of the paper are as follows.

1) The 1980-2017 pre- and post-monsoon-onset periods consist of 49.6 and 41.4 days per year on average, respectively. Under the more favorable thermodynamic and moisture conditions over South China after the SCS

monsoon onset, the daily rainfall amount and period-accumulated rainfall amount increase by 30.4% and 8.3%, respectively. Hourly rainfall rate of the rainfall events also intensifies by 26.5%, while the events' average duration (4.3 vs. 4.2 h) becomes slightly shorter due to an increased population of short-duration (1-6 h) rainfall events after the SCS monsoon onset.

2) After the SCS monsoon onset, hourly rainfall intensities of the short-, moderate-, and long-duration events are all enhanced, with more significant increase in the longer-duration (> 6 h) categories over the west-inland region. Compared to the pre-monsoon-onset period, the rainfall events occur more (less) frequently over the west-inland and coastal regions (northern portion of the east-inland region), resulting in a substantial increase (little change) in total rainfall amounts after the monsoon onset over these two regions (east-inland region).

3) The long-duration rainy days over the inland SC regions are closely linked to subtropical synoptic systems (i.e., low pressure and an associated front or shearline) and southwesterly air flow of tropical origin, which together provide favorable dynamic instability and thermodynamic conditions for the rainfall production. The westward extension of the western North Pacific high (WNPH) and the eastward extension/movement of the front/shearline, interacting with the intra-period intensification of the southwesterly monsoonal flows, play important roles in providing high-$\theta_e$ air to the west- and east-inland regions, respectively.

4) About 64% of the coastal long-duration rainy days is concurrent with the inland long-duration rainy days. The warm-sector, coastal rainfall is closely related to the deceleration of the southerly BL flow over northern SCS and the associated convergence of BL high-$\theta_e$ air near the coast. The coastal rainfall can also be aided by the SLLJ in the lower-to-middle troposphere that provides divergence aloft with BL convergence near the coast.

To conclude, this study provides quantitative analysis of characteristics of pre-summer rainfall over SC and the associated synoptic conditions. The 38-year statistical analysis not only supports but also expands upon previous studies showing qualitative results or focusing on single heavy-rainfall case over SC. Properties of the double LLJs (BLJ, SLLJ), their possible interactions, as well as their relationship with heavy rainfall over SC, deserve further investigation through more detailed analysis using observations and re-analysis data, combined with carefully designed numerical simulations.

## Acknowledgements

We would like to thank two anonymous reviewers and the editor for their constructive comments, which have helped us substantially in improving the manuscript. We also thank Prof. Richard H. Johnson (Colorado State University) for editing the manuscript. This research is supported by the National (Key) Basic Research and Development Program of China (2018YFC1507400), the National Natural Science Foundation of China (41775050 and 41875055), and the Basic Research & Operation Funding of Chinese Academy of Meteorological Sciences (CAMS) (2017Z006).

## References

Charney, J. G., and M. E. Stern, 1962: On the stability of internal baroclinic jets in a rotating atmosphere. *J. Atmos. Sci.*,**19**, 159–172.

Chen, Y. and Y. Luo, 2018. Analysis of paths and sources of moisture for the South China rainfall during the presummer rainy season of 1979-2014. *J. Meteor. Res.*, **32**, 744-757.

Chen, X., F. Zhang and K. Zhao, 2016: Diurnal variations of the land–sea breeze and its related precipitation over South China. *J. Atmos. Sci.*, **73**, 4793-4815.

Chen, X., F. Zhang, and K. Zhao, 2017: Influence of monsoonal wind speed and moisture content on intensity and diurnal variations of the mei-yu season coastal rainfall over South China. *J. Atmos. Sci.*, **74**, 2835–2856.

Dai, A., F. Giorgi, and K. E. Trenberth, 1999: Observed and model simulated diurnal cycles of precipitation over the contiguous United States. *J. Geophys. Res.*, **104**, 6377–6402.

Dee, D. P., and Coauthors, 2011: The ERA-Interim reanalysis: Configuration and performance of the data assimilation system. *Quart. J. Roy. Meteor. Soc.*, **137**, 553–597.

Ding, Y., 1994: Monsoons over China. Kluwer Academic, 419 pp.

Ding, Y., and J. C. L. Chan, 2005: The East Asian summer monsoon: An overview. *Meteor. Atmos. Phys.*, **89**, 117–142.

Du, Y. and G. Chen, 2018: Heavy rainfalls associated with double low-level jets over Southern China. Part I: Ensemble-based analysis. *Mon. Wea. Rev.,* **146**, 3827–3844.

Du, Y. and G. Chen, 2019: Heavy rainfalls associated with double low-level jets over Southern China. Part II: Convection initiation. *Mon. Wea. Rev.*, **147**, 543-565.

Du, Y., Q. H. Zhang, Y. Ying, Y. Y. Zhao, and X. Wang, 2014: Numerical simulations of spatial distributions and diurnal variations of low-level jets in China during early summer. *J. Climate*, **27**, 5747-5767.

Du, Y., Q. H. Zhang, Y. Ying, and Y. M. Yang, 2012: Characteristics of low-level jets in Shanghai during the 2008–2009 warm seasons as inferred from wind profiler radar data. *J. Meteor. Soc. Japan*, **90**, 891–903.

Guo, J., T. Su, and Coauthors, 2017: Declining frequency of summertime local-scale precipitation over eastern China from 1970 to 2010 and its potential link to aerosols. *Geophys. Res. Lett.*, **44**, 5700–5708.

Hallegatte, S., C. Green, R. J. Nicholls, and J. Corfee-Morlot, 2013: Future flood losses in major coastal cities. *Nature Clim. Change*, **3**, 802–806.

Hastenrath, S., 1985: *Climate and Circulation of the Tropics*. D. Reidel Publishing Company, 455 pp.

Holton, J. R., 2004: *An Introduction to Dynamic Meteorology*. Elsevier Academic Press, 535 pp.

Huang, Y., Y. Liu, Y. Liu, and Coauthors, 2019: Mechanisms for a record-breaking rainfall in the coastal metropolitan city of Guangzhou, China:

Observation analysis and nested very large eddy simulation with the WRF model. *J. Geophys. Res. Atmos.*, **124**, 1370–1391.

Huang, L., and Y. Luo, 2017: Evaluation of quantitative precipitation forecasts by TIGGE ensembles for south China during the presummer rainy season. *J. Geophys. Res. Atmos.*, **122**, 8494–8516.

Huang, L., Y. Luo, and D. L. Zhang, 2018: The relationship between anomalous pre-summer extreme rainfall over south China and synoptic disturbances. *J. Geophys. Res. Atmos.*, **123**, 3395-3413.

Huang, S. S., and Coauthors, 1986: *Heavy Rainfall over Southern China in the Pre-Summer Rainy Season* (in Chinese). Guangdong Science and Technology Press, 244 pp.

Huang, D., J. Zhu, Y. Zhang, J. Wang, and X. Kuang, 2015: The impact of the East Asian subtropical jet and polar front jet on the frequency of spring persistent rainfall over southern China in 1997-2011. *J. Climate*, **28**, 6054-6066.

Jiang, Z., D.-L. Zhang, R. Xia, and T. Qian, 2017: Diurnal variations of presummer rainfall over southern China. *J. Climate*, **30**, 755–773.

Keyser, D., and M. A. Shapiro, 1986: A review of the structure and dynamics of upper-level frontal zones. *Mon. Wea. Rev.*, **114**, 452–499.

Kummerow, C., W. Barnes, T. Kozu, J. Shiue, and J. Simpron, 1998: The Tropical Rainfall Measuring Mission (TRMM) sensor package. *J. Atmos. Oceanic Technol.*, **15**, 809–817.

Lau, K. M., Y. Ding, J.-T. Wang, and Coauthors, 2000: A Report of the Field Operations and Early Results of the South China Sea Monsoon Experiment (SCSMEX). *Bull. Amer. Meteor. Soc.*, **81**, 1261-1270.

Li, X., Y. Luo, and Z. Guan, 2014: The persistent heavy rainfall over southern China in June 2010: Evolution of synoptic systems and the effects of the Tibetan Plateau heating. *J. Meteor. Res.*, **28**, 540–560.

Li, J., R. Yu, and W. Sun, 2013: Duration and seasonality of hourly extreme rainfall in the central eastern China. *Acta Meteor. Sin.*, **27**, 799–807.

Li, J., R. Yu, and T. Zhou, 2008: Seasonal variation of the diurnal cycle of rainfall in southern contiguous China. *J. Clim.*, **21**, 6036–6043.

Liu, X., Y. Luo, Z. Guan, and D.-L. Zhang, 2018: An extreme rainfall event in coastal South China during SCMREX-2014: Formation and roles of Rainband and Echo trainings. *J. Geophys. Res. Atmos.*, **123**, 9256–9278.

Luo, Y., 2017: Advances in understanding the early-summer heavy rainfall over South China. *The Global Monsoon System: Research and Forecast (3rd Edition)*. Editors: C.P. Chang, N. G. Lau, R. H. Johnson, B. Wang and M. Wheeler. World Scientific Series on Asia-Pacific Weather and Climate, Vol. **9**, 215-226.

Luo, Y., R. Zhang, Q. Wan, and Coauthors, 2017: The Southern China Monsoon Rainfall Experiment (SCMREX). *Bull. Amer. Meteor. Soc.*, **98**, 999–1013.

Luo, Y., M. Wu, F. Ren, J. Li, and W. K. Wong, 2016: Synoptic situations of extreme hourly precipitation over China. *J. Climate*, **29**,8703–8719.

Luo, Y., H. Wang, R. Zhang, W. Qian, and Z. Luo, 2013: Comparison of rainfall characteristics and convective properties of monsoon precipitation systems over South China and the Yangtze and Huai River Basin. *J. Climate*, **26**, 110–132.

Pham, N. T., K. Nakamura, F. A. Furuzawa, and S. Satoh, 2008: Characteristics of low level jets over Okinawa in the Baiu and post-Baiu seasons revealed by wind profiler observations. *J. Meteor. Soc. Japan*, **86**, 699–717.

Ramage, C. S., 1952: Variation of rainfall over South China through the wet season. *Bull. Amer. Meteor. Soc.*, **33**, 308–311.

Tian, S., and T. Yasunari, 1998: Climatological aspects and mechanisms of spring persistent rains over central China. *J. Meteor. Soc. Japan*, **76**, 57–71.

Tu, C.-C., Y.-L. Chen, C.-S. Chen, P.-L. Lin, and P.-H. Lin, 2014: A comparison of two heavy rainfall events during the Terrain Influenced Monsoon Rainfall Experiment (TiMREX) 2008. *Mon. Wea. Rev.*, **142**, 2436–2463.

Wang, H., Y. Luo, and B. J.-D. Jou, 2014: Initiation, maintenance, and properties of convection in an extreme rainfall event during SCMREX: Observational analysis. *J. Geophys. Res. Atmos.*, **119**, 13,206-13,232.

Whiteman, C. D., X. Bian, and S. Zhong, 1997: Low-level jet climatology from enhanced rawinsonde observations at a site in the southern Great Plains. *J. Appl. Meteor.*, **36**, 1363–1376.

Wu, G., Y. Liu, Q. Zhang, and Coauthors, 2007: The influence of mechanical and thermal forcing by the Tibetan Plateau on Asian climate. *J. Hydrometer.*, **8**, 770-789.

Wu, M., and Y. Luo, 2016: Mesoscale observational analysis of lifting mechanism of a warm-sector convective system producing the maximal daily precipitation in China mainland during pre-summer rainy season of 2015. *J. Meteor. Res.*, **30**, 719–736.

Wu, M., Y. Luo, F. Chen, and W.-K. Wong, 2019: Observed Link of Extreme Hourly Precipitation Changes to Urbanization over Coastal South China. *J. Appl. Meteor. Climate*, In press.

Xie, A., Y. Chung, X. Liu, and Q. Ye, 1998: The interannual variations of the summer monsoon onset over the South China Sea. *Theor. Appl. Climatol.*, **59**, 201–213.

Xu, W., E. J. Zipser, and C. Liu, 2009: Rainfall characteristics and convective properties of mei-yu precipitation systems over South China, Taiwan, and the South China Sea. Part I: TRMM observations. *Mon. Wea. Rev.*, **137**, 4261–4275.

Yu, R., Y. Xu, T. Zhou, and J. Li, 2007: Relation between rainfall duration and diurnal variation in the warm season precipitation over central eastern China. *Geophys. Res. Lett.*, **34**, L13703, doi:10.1029/2007GL030315.

Yu, R., W. Yuan, and J. Li, 2013: The asymmetry of rainfall process. *Chin. Sci. Bull.*, **58**, 1850–1856.

Yuan, F., K. Wei, W. Chen, S. K. Fong, and K. C. Leong, 2010: Temporal variations of the frontal and monsoon storm rainfall during the first rainy season in South China. *Atmos. Oceanic Sci. Lett.*, **3**, 243–247.

Zhang, M., and Z. Meng, 2018: Impact of synoptic-scale factors on rainfall forecast in different stages of a persistent heavy rainfall event in South China. *J. Geophys. Res. Atmos.*, **123**, 3574– 3593.

Zhao, P., R. Zhang, J. Liu, X. Zhou, and J. He, 2007: Onset of southwesterly wind over eastern China and associated atmospheric circulation and rainfall. *Clim. Dyn.*, **28**, 797–811.

Zhao, P., X. Zhou, L. Chen, and J. He, 2008: Characteristics of subtropical monsoon and rainfall over eastern China and western North Pacific and associated reasons. *Acta Meteorologica Sinica*, **66**(6), 940-954.

Zhao, P., J. Sun, and X. Zhou, 2003: Mechanism of formation of low level jets in the South China Sea during spring and summer of 1998. *Chinese Sci. Bull.*, **12**, 1265-1270.

Zhao, S. X., N. F. Bei, and J. H. Sun, 2007: Mesoscale analysis of a heavy rainfall event over Hong Kong during a pre-rainy season in South China. *Adv. Atmos. Sci.*, 24, 555–572.

Zheng, Y., M. Xue, B. Li, J. Chen, and Z. Tao, 2016: Spatial characteristics of extreme rainfall over China with hourly through 24-hour accumulation periods based on national-level hourly rain gauge data. *Adv. Atmos. Sci.*, **33**, 1218–1232.

# Figure Captions

Fig. 1 Topographical (m) map of southern China. Locations of Guangdong (GD), Guangxi (GX), Guizhou, Hunan, Jiangxi, Fujian, Yunnan Provinces and Hainan island are labeled. Gray lines denote the province borders. Blue dots designate 303 meteorological surface stations. South China (SC) defined in the study is the regions within the large purple box (19°-27°N, 105°-118°E). The outlined boxes A, B, and C denote the west-inland, east-inland, and coastal regions; similarly used in the subsequent figures. The dashed box indicates the region used to analyze the low-level jets.

Fig. 2 Numbers of the long-duration rainy days over the west-inland (red), east-inland (blue), and coastal regions (green) during the pre-monsoon-onset (left) and post-monsoon-onset (right) periods. The overlapping parts denote concurrences of the long-duration rainy days over two or three regions.

Fig. 3 Box-and-whisker plots of (a) rainfall amount, (b) occurrence frequency, and (c) average intensity for the short-, moderate-, and long-duration rainfall events at the 303 stations over South China during the pre-monsoon-onset (red) and post-monsoon-onset (blue) periods. The middle dot represents the mean value of the 303 stations, short line in the box represents the median, top and bottom of the box indicate the interquartile range, upper (lower) short line denotes the $90^{th}$ ($10^{th}$) percentile, and top (bottom) dot shows the maximum (minimum) of all the stations. The values of "zero" appear in the long-duration rainfall events because there are two stations without a long-duration rainfall event during the pre-monsoon-onset period.

Fig. 4 Histograms of the station-based rainfall amount (gray bars) and its cumulative distribution function (CDF; red line) of all rainfall events during the (a) pre-monsoon-onset period and (b) post-monsoon-onset period. Spatial distribution of rainfall amount (mm $day^{-1}$) during (c) the pre-monsoon-onset period, (d) the post-monsoon-onset period, and (e) the difference between the two periods (the rainfall amount during the latter period minus the rainfall amount during former period).

The west-inland, east-inland, and coastal regions are outlined by solid lines.

Fig. 5 As in Fig. 4, but for the occurrence frequency of the rainfall events.

Fig. 6 Spatial distribution of occurrence frequency (# per day) during the pre-monsoon-onset period (left column), post-monsoon-onset period (middle column), and the difference between the two periods (post- minus pre-monsoon-onset period) (right column) for the three rainfall-event types with short-, moderate-, and long-duration (from top to bottom), respectively. The hollow circles over Hainan island in (c) indicate two stations not having any long-duration rainfall event.

Fig. 7 As in Fig. 4, but for the average intensity of the rainfall events.

Fig. 8 (a-c) Composite fields at 850 hPa averaged on the long-duration rainy days over (a) only the west-inland region, (b) both the west- and east-inland regions, and (c) only the east-inland region during the pre-monsoon-onset period: equivalent potential temperature ($\theta_e$, green solid, contoured at intervals of 4 K), geopotential height (black solid, contoured at intervals of 10 gpm), horizontal winds (vectors; red denotes wind speed $\geqslant$5 m $s^{-1}$), and precipitable water (mm, blue shadings). The regions are outlined by pink quadrilaterals. The orange lines indicate the shearlines in the average wind fields and the red contours represent the standard deviation of meridional velocity ($v$). (d-f) Anomalous fields of the 850hPa $\theta_e$ (green solid, contoured at intervals of 1 K), relative vorticity (red solid, $10^{-6}$ $s^{-1}$), horizontal winds (vectors), and precipitable water (mm, blue shadings) during the pre-monsoon-onset period corresponding to (a), (b), and (c), respectively. The anomalies are calculated as the averages on the long-duration rainy days over the inland region(s) minus the climatological (1980-2017) averages during the pre-monsoon-onset period, i.e., the averages over all the 6-hourly re-analysis data during the pre-monsoon-onset periods of 1980-2017.Fig. 9 As in Fig. 8, but during the post-monsoon-onset period.

Fig. 10 Composite fields at 925 hPa averaged on the long-duration rainy days over (a) both the coastal and east-inland regions, (b) only the coastal region during the pre-monsoon-onset period: equivalent potential temperature ($\theta_e$; green solid, contoured at intervals of 4 K), geopotential height (black solid, contoured at intervals of 10 gpm), horizontal winds (vectors; red denotes wind speed $\geqslant$5 m $s^{-1}$), and wind convergence (red solid, $10^{-6}$ $s^{-1}$), overlaid by vertically integrated precipitable water (mm, blue shadings). The regions are outlined by pink rectangles. (c) and (d) Similar to (a) and (b), but at 850 hPa. The brown meridional line in (b) is used in the analysis of Figs. 12--14.

Fig. 11 As in Fig. 10, but during the post-monsoon-onset period.

Fig. 12 Vertical cross sections of meridional wind speed (shading), in-plane flow vectors (black vectors; the vertical velocity is multiplied by 200), convergence (black solid; contoured at intervals of $-4\times10^{-6}$ $s^{-1}$) and divergence (white solid; contoured at intervals of $2\times10^{-6}$ $s^{-1}$) along the brown line in Fig. 10b. The variables are averaged on the long-duration rainy days over both the coastal and east-inland regions (a and d), over the coastal region only (b and e), and on the days without rainfall over the coastal region (c and f). Left and right panels show the results during the pre- and post-monsoon-onset periods, respectively. Blue triangle indicates location of the coastline.

Fig. 13 Vertical cross sections of meridional wind speed (shading), in-plain flow vectors (black vectors; the vertical velocity is multiplied by 200), convergence (black solid; contoured at intervals of $-4\times10^{-6}$ $s^{-1}$) and divergence (white solid; contoured at intervals of $2\times10^{-6}$ $s^{-1}$) along the brown line in Fig. 10b. The variables are averaged for two subgroups of the long-duration rainy days over both the coastal and east-inland regions, i.e., (a-b) with and (c-d) without the BLJ events, respectively. (a) and (c) show the results during the pre-monsoon-onset period and (b) and (d) the post-monsoon-onset period. Blue triangle indicates location of the coastline.

Fig. 14 As in Fig. 13, but for the long-duration rainy days over the coastal region only.

Table 1. Statistics of presummer rainfall over South China during the pre- and post-monsoon-onset periods of 1980-2017. Numbers in brackets represent the change (%) relative to the pre-monsoon-onset period.

| | **Pre-monsoon-onset period** | **Post-monsoon-onset period** |
|---|---|---|
| Span of the period (day $year^{-1}$) | 49.6 | 41.4 [-16.5%] |
| Accumulated rainfall amount (mm $year^{-1}$) | 277.1 | 300.2 [+8.3%] |
| Occurrence frequency of rainfall event (# $year^{-1}$) | 35.5 | 31.1 [-12.4%] |
| Daily rainfall amount (mm) | 5.6 | 7.3 [+30.4%] |
| Daily occurrence frequency of rainfall event (#) | 0.72 | 0.75 [+4.2%] |
| Average duration of rainfall event (hour) | 4.3 | 4.2 [-2.3%] |
| Average intensity of hourly rainfall (mm $hour^{-1}$) | 1.81 | 2.29 [+26.5%] |

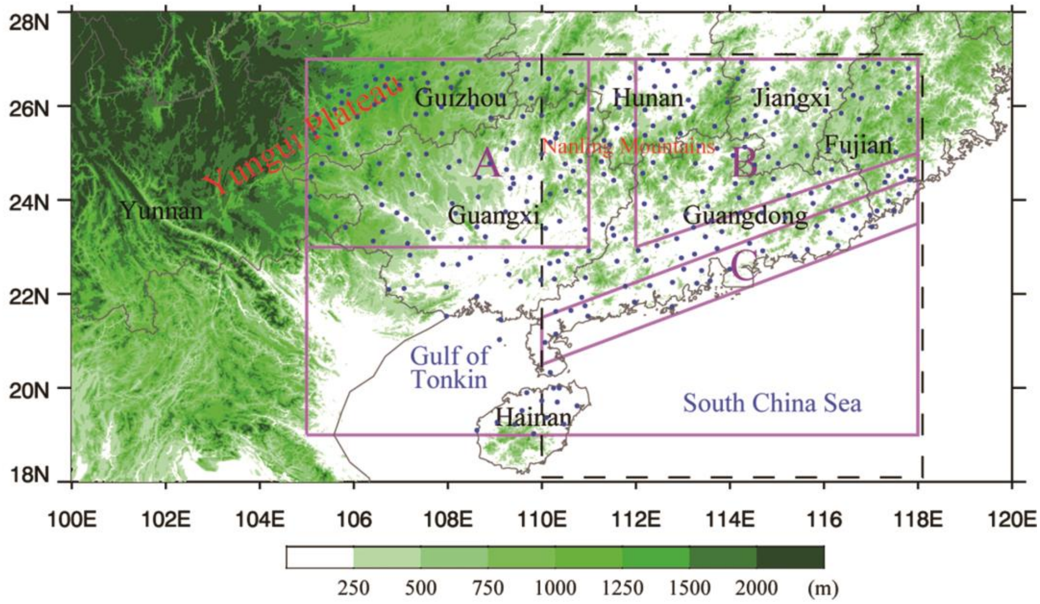


Fig. 1 Topographical (m) map of southern China. Locations of Guangdong (GD), Guangxi (GX), Guizhou, Hunan, Jiangxi, Fujian, Yunnan Provinces and Hainan island are labeled. Gray lines denote the province borders. Blue dots designate 303 meteorological surface stations. South China (SC) defined in the study is the regions within the large purple box (19°-27°N, 105°-118°E). The outlined boxes A, B, and C denote the west-inland, east-inland, and coastal regions; similarly used in the subsequent figures. The dashed box indicates the region used to analyze the low-level jets.

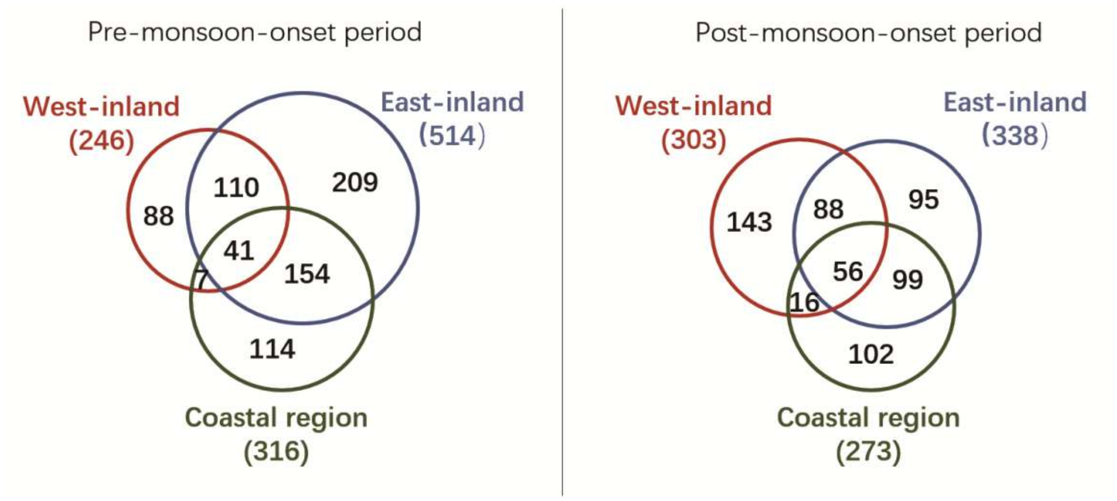


Fig. 2 Numbers of the long-duration rainy days over the west-inland (red), east-inland (blue), and coastal regions (green) during the pre-monsoon-onset (left) and post-monsoon-onset (right) periods. The overlapping parts denote concurrences of the long-duration rainy days over two or three regions.

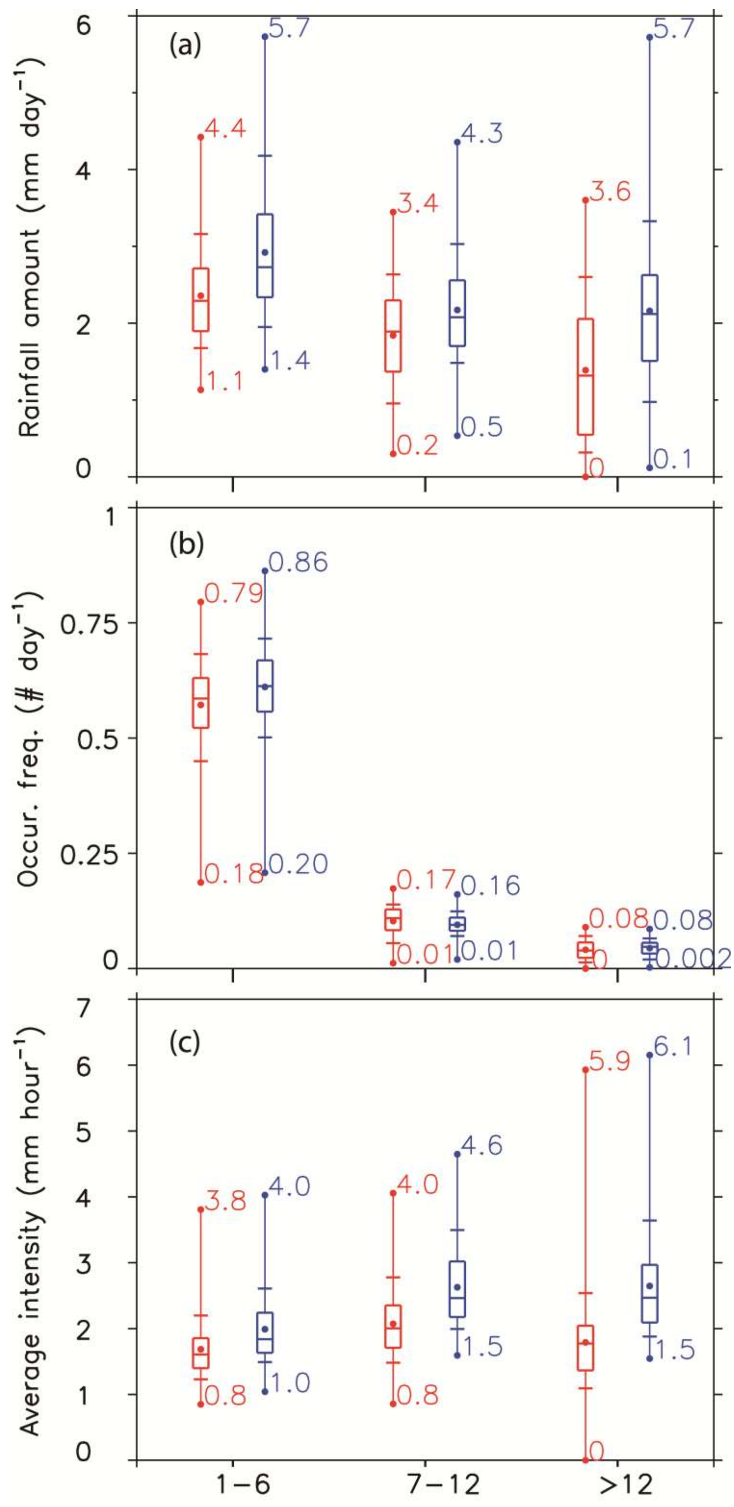


Fig. 3 Box-and-whisker plots of (a) rainfall amount, (b) occurrence frequency, and (c) average intensity for the short-, moderate-, and long-duration rainfall events at the 303 stations over South China during the pre-monsoon-onset (red) and post-monsoon-onset (blue) periods. The middle dot represents the mean value of the 303 stations, short line in the box represents the median, top and bottom of the box indicate the interquartile range, upper (lower) short line denotes the 90$^{th}$ (10$^{th}$) percentile, and top (bottom) dot

shows the maximum (minimum) of all the stations. The values of “zero” appear in the long-duration rainfall events because there are two stations without a long-duration rainfall event during the pre-monsoon-onset period.

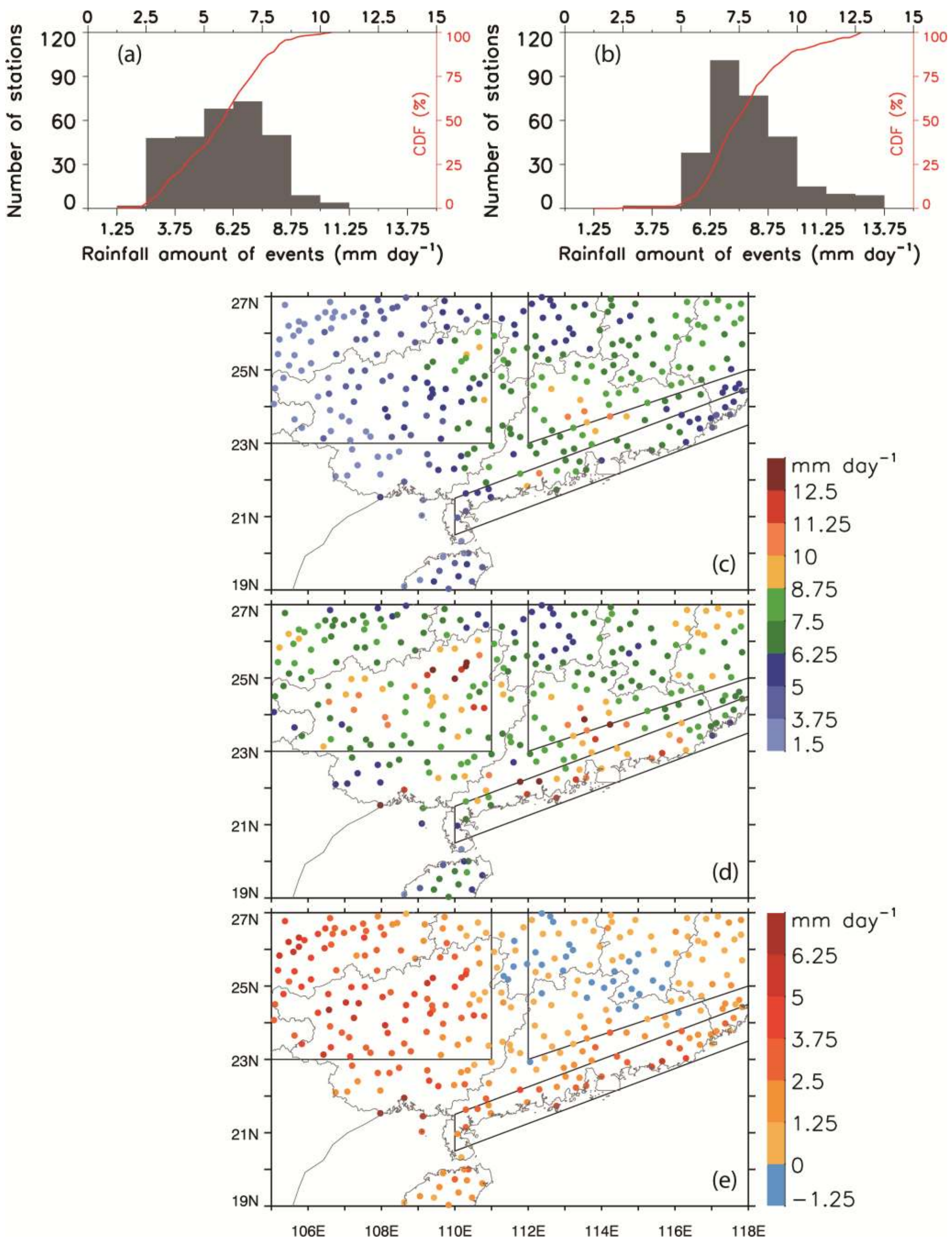


Fig. 4 Histograms of the station-based rainfall amount (gray bars) and its cumulative distribution function (CDF; red line) of all rainfall events during the (a) pre-monsoon-onset period and (b) post-monsoon-onset period. Spatial distribution of rainfall amount (mm day$^{-1}$) during (c) the pre-monsoon-onset period, (d) the post-monsoon-onset period, and (e) the difference between the two periods (the rainfall amount during the latter period minus the rainfall amount during former period). The west-inland, east-inland, and coastal regions are outlined by solid lines.

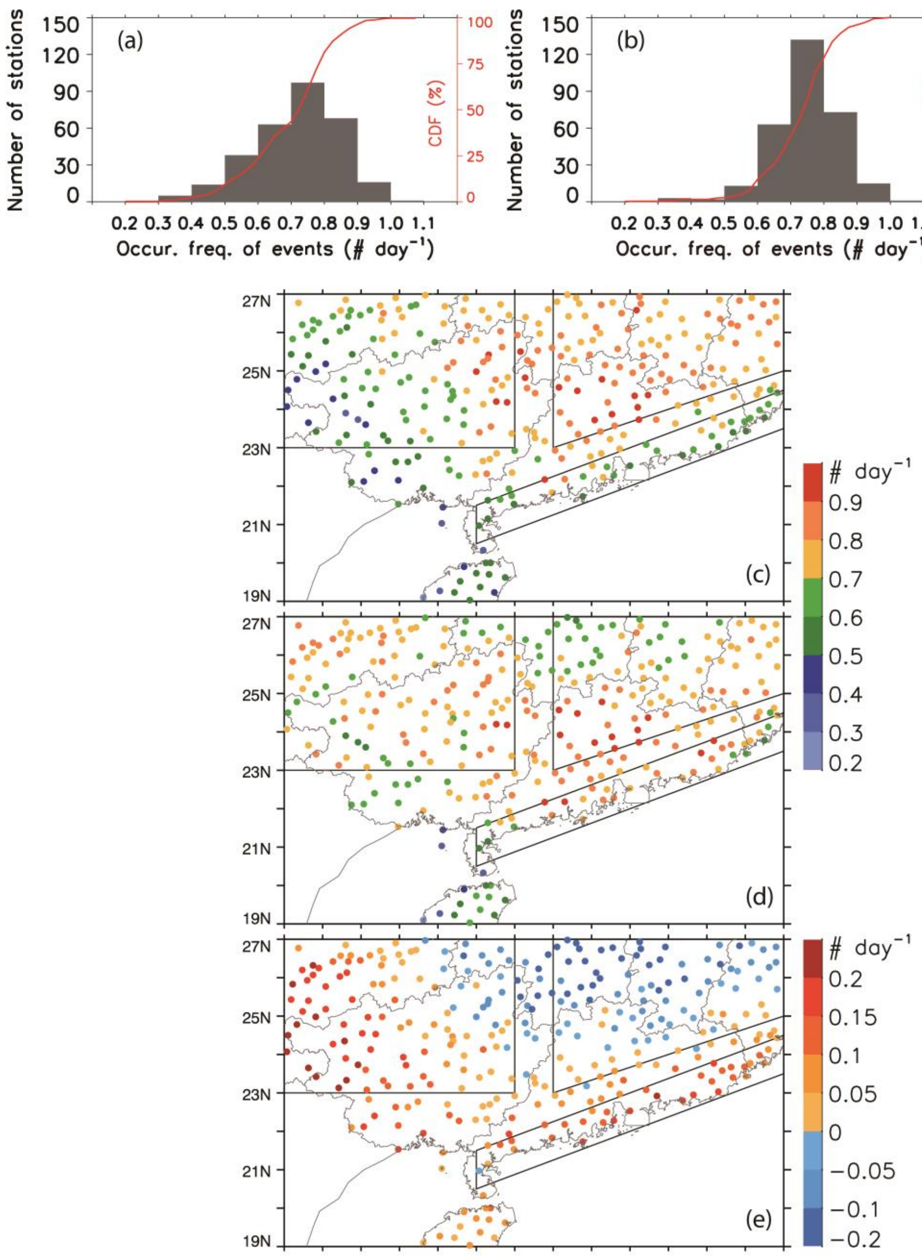


Fig. 5 As in Fig. 4, but for the occurrence frequency of the rainfall events.

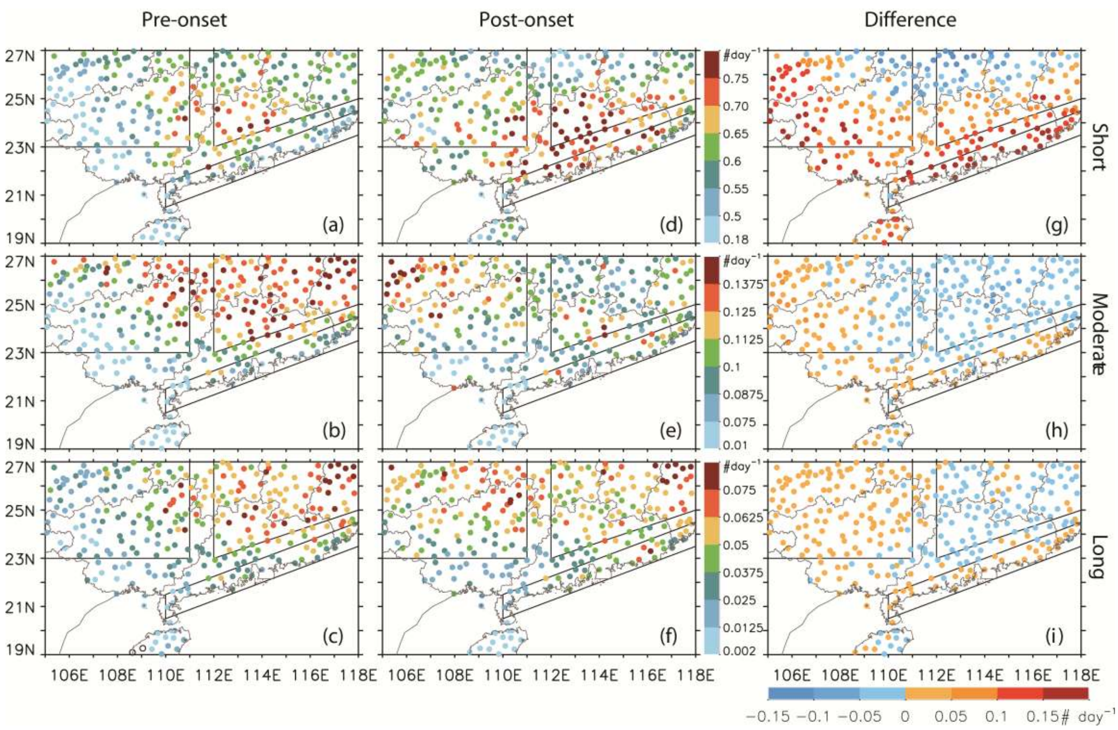


Fig. 6 Spatial distribution of occurrence frequency (# per day) during the pre-monsoon-onset period (left column), post-monsoon-onset period (middle column), and the difference between the two periods (post- minus pre-monsoon-onset period) (right column) for the three rainfall-event types with short-, moderate-, and long-duration (from top to bottom), respectively. The hollow circles over Hainan island in (c) indicate two stations not having any long-duration rainfall event.

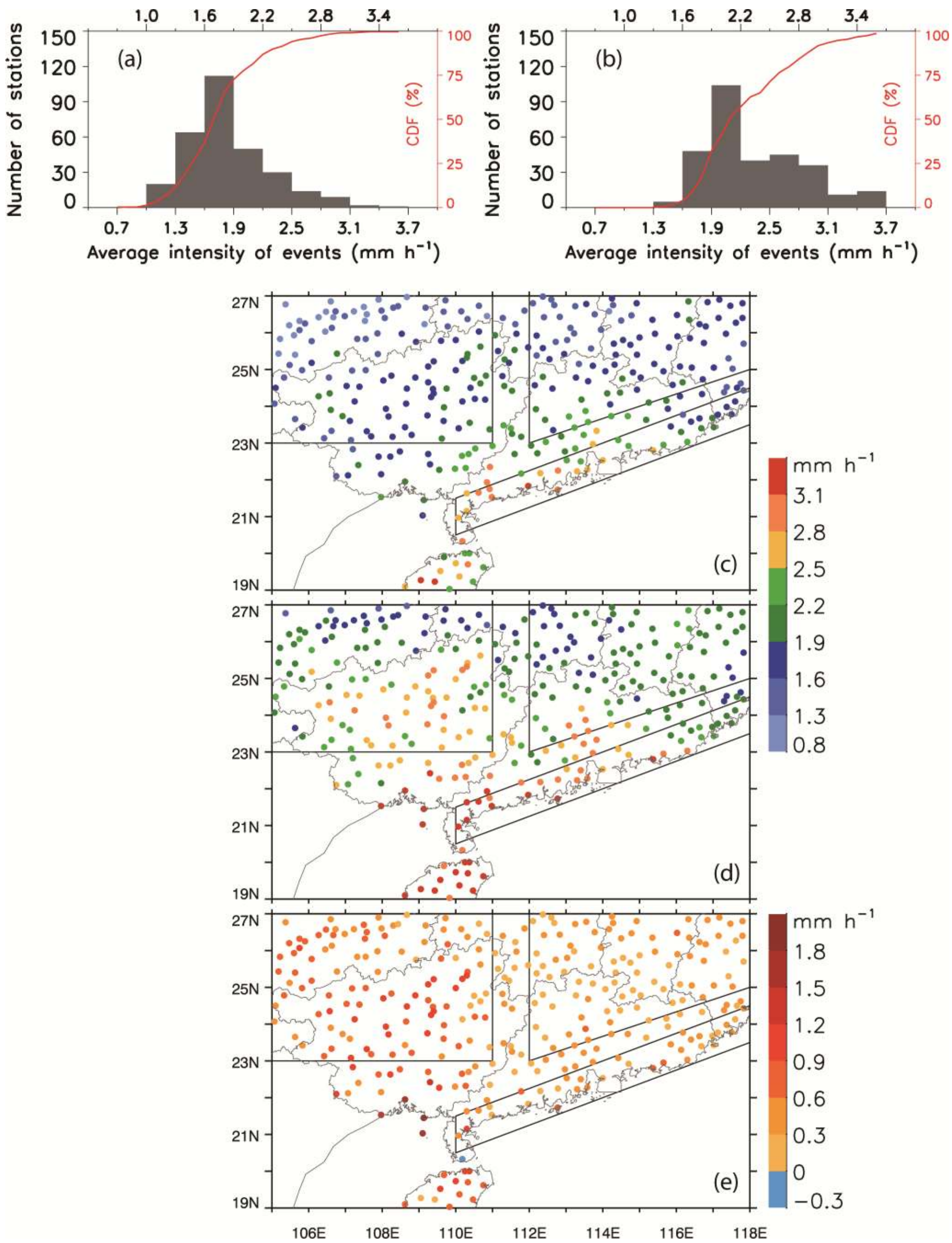


Fig. 7 As in Fig. 4, but for the average intensity of the rainfall events.

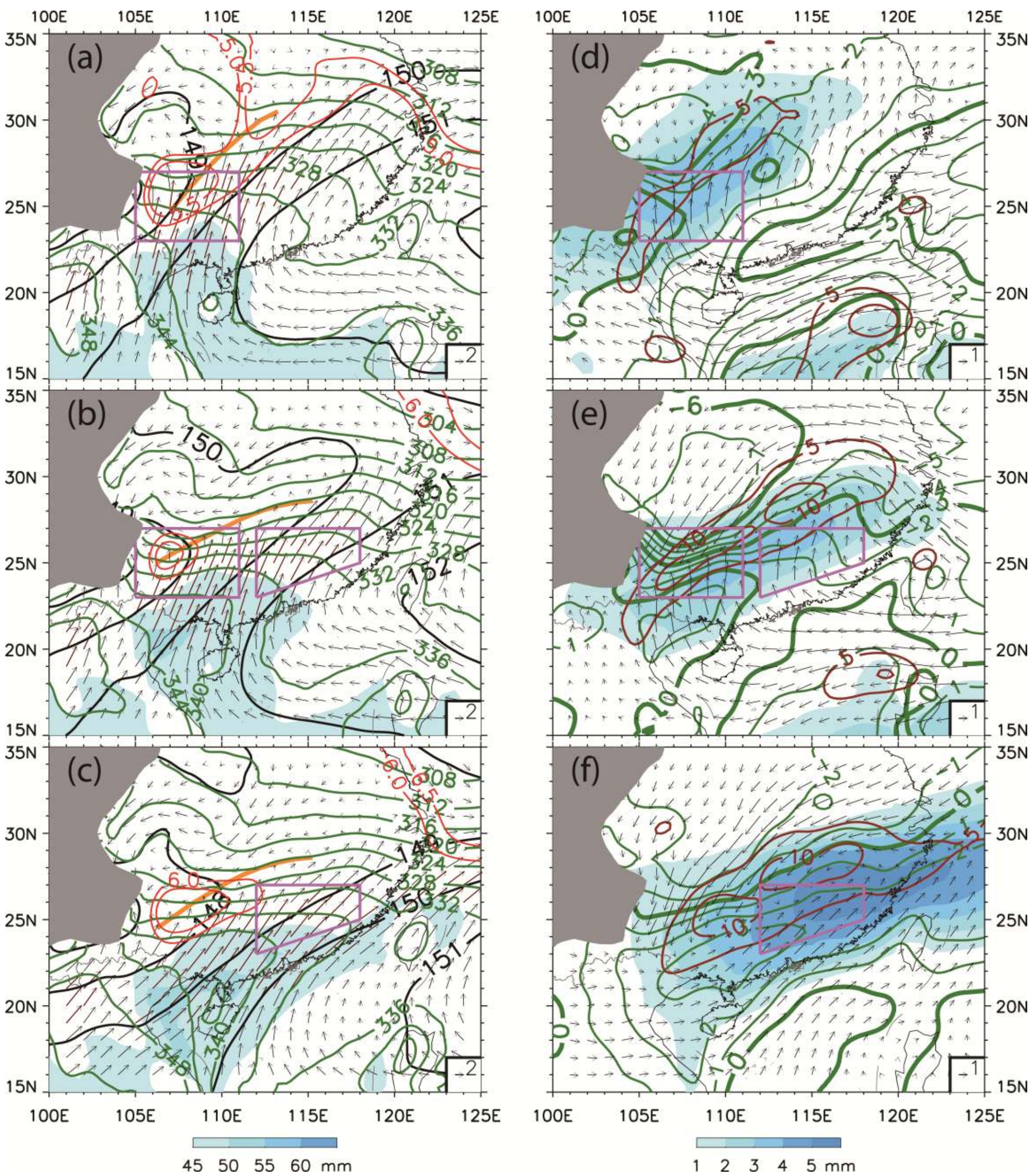


Fig. 8 (a-c) Composite fields at 850 hPa averaged on the long-duration rainy days over (a) only the west-inland region, (b) both the west- and east-inland regions, and (c) only the east-inland region during the pre-monsoon-onset period: equivalent potential temperature ($\theta_e$, green solid, contoured at intervals of 4 K), geopotential height (black solid, contoured at intervals of 10 gpm), horizontal winds (vectors; red denotes wind speed $\geqslant 5$ m $s^{-1}$), and precipitable water (mm, blue shadings). The regions are outlined by pink quadrilaterals. The orange lines indicate the shearlines in the average wind fields and the red contours represent the standard deviation of meridional velocity (*v*). (d-f) Anomalous fields of the 850hPa $\theta_e$ (green solid, contoured at intervals of 1 K), relative vorticity (red solid, $10^{-6}$ $s^{-1}$), horizontal winds (vectors), and precipitable water (mm, blue shadings) during the pre-monsoon-onset period corresponding to (a), (b), and (c), respectively. The anomalies are calculated as the averages on the long-duration rainy days over the inland region(s) minus the climatological (1980-2017) averages during the pre-monsoon-onset period, i.e., the averages over all the 6-hourly re-analysis data during the pre-monsoon-onset periods of 1980-2017.

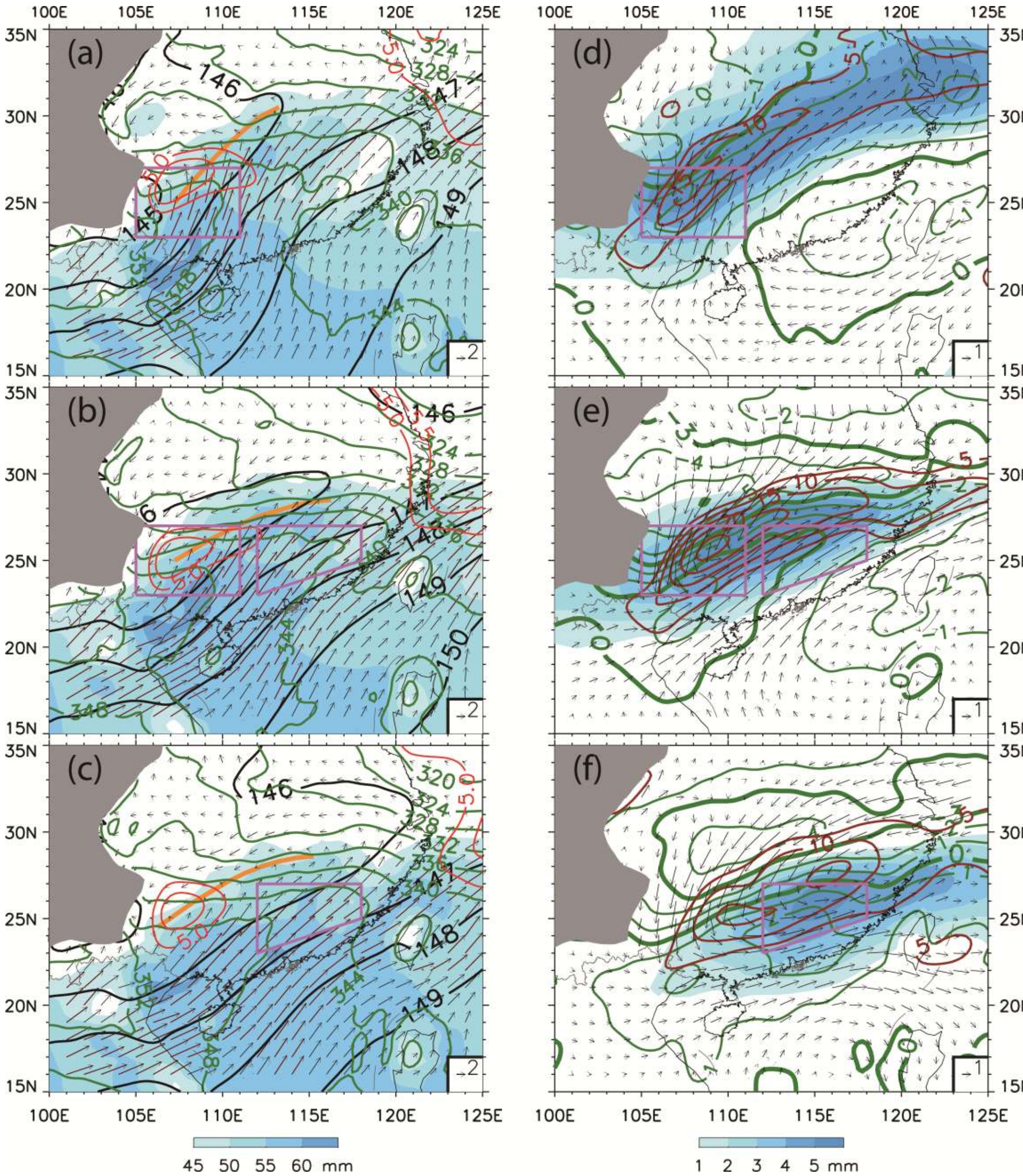


Fig. 9 As in Fig. 8, but during the post-monsoon-onset period.

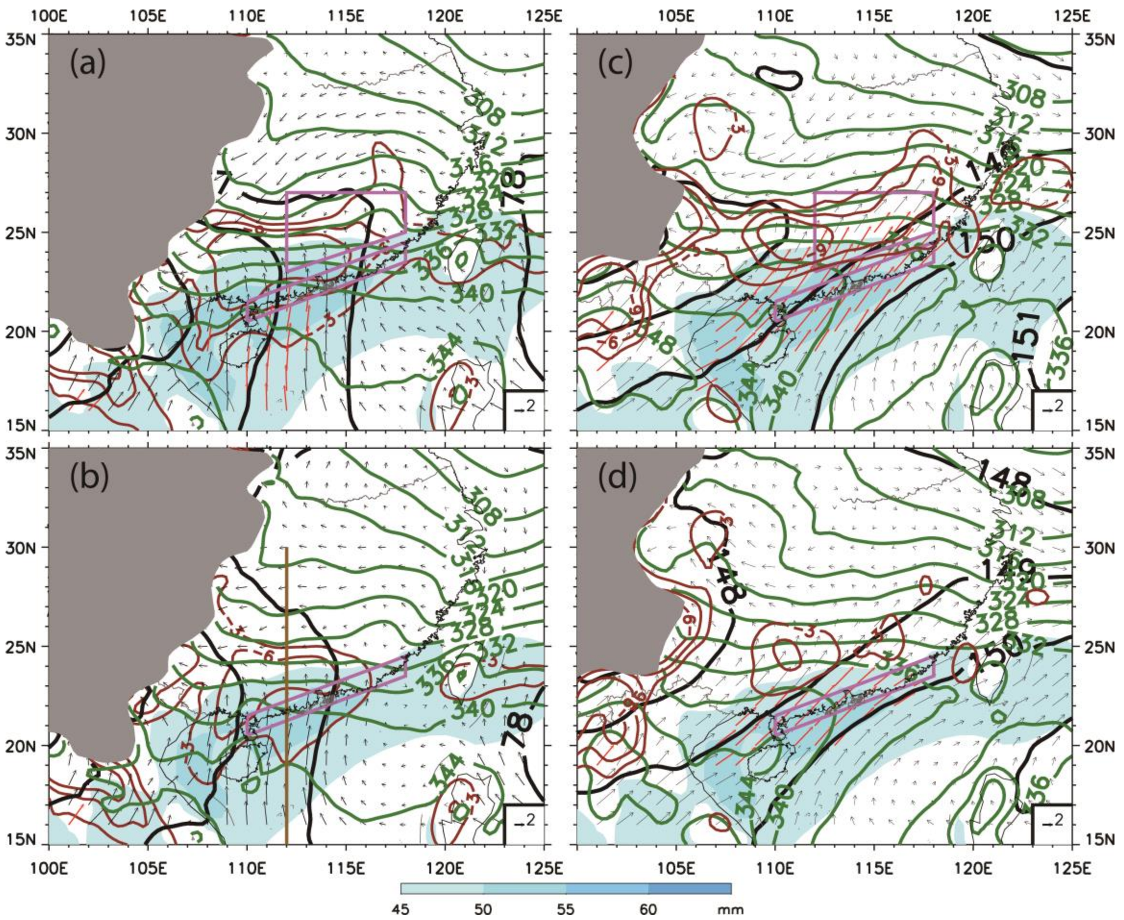


Fig. 10 Composite fields at 925 hPa averaged on the long-duration rainy days over (a) both the coastal and east-inland regions, (b) only the coastal region during the pre-monsoon-onset period: equivalent potential temperature ($\theta_e$; green solid, contoured at intervals of 4 K), geopotential height (black solid, contoured at intervals of 10 gpm), horizontal winds (vectors; red denotes wind speed $\geq$5 m $s^{-1}$), and wind convergence (red solid, $10^{-6}$ $s^{-1}$), overlaid by vertically integrated precipitable water (mm, blue shadings). The regions are outlined by pink rectangles. (c) and (d) Similar to (a) and (b), but at 850 hPa. The brown meridional line in (b) is used in the analysis of Figs. 12-14.

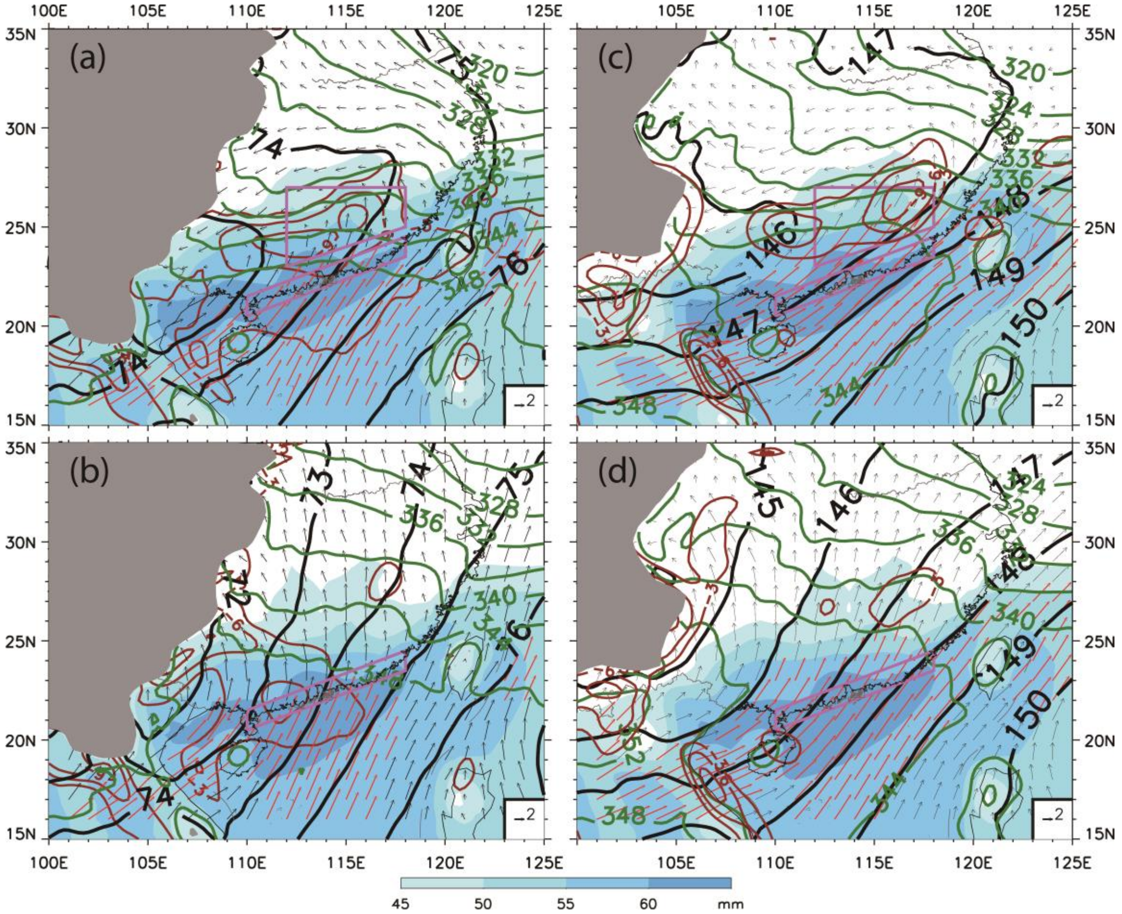


Fig. 11 As in Fig. 10, but during the post-monsoon-onset period.

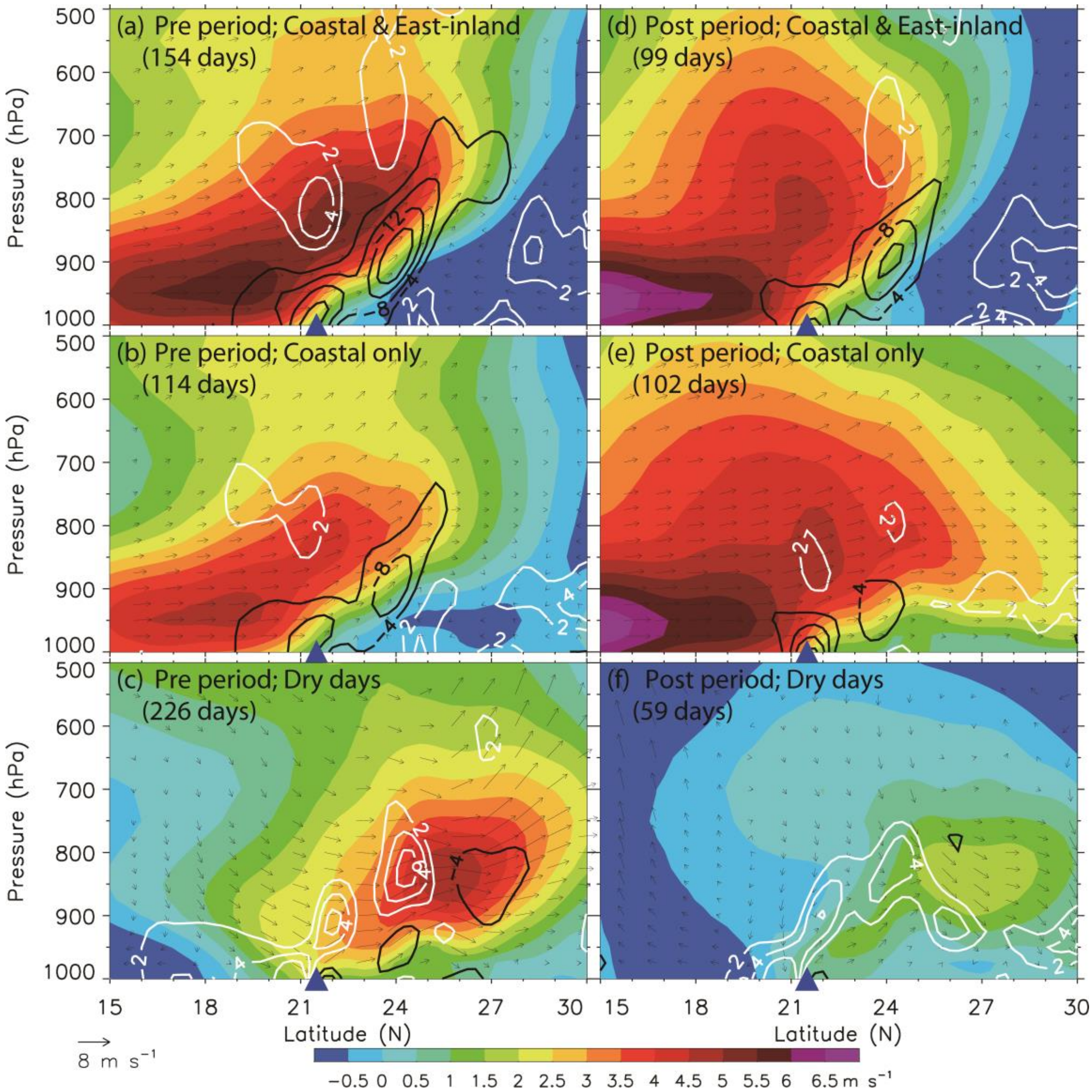


Fig. 12 Vertical cross sections of meridional wind speed (shading), in-plane flow vectors (black vectors; the vertical velocity is multiplied by 200), convergence (black solid; contoured at intervals of $-4\times10^{-6}$ $s^{-1}$) and divergence (white solid; contoured at intervals of $2\times10^{-6}$ $s^{-1}$) along the brown line in Fig. 10b. The variables are averaged on the long-duration rainy days over both the coastal and east-inland regions (a and d), over the coastal region only (b and e), and on the days without rainfall over the coastal region (c and f). Left and right panels show the results during the pre- and post-monsoon-onset periods, respectively. Blue triangle indicates location of the coastline.

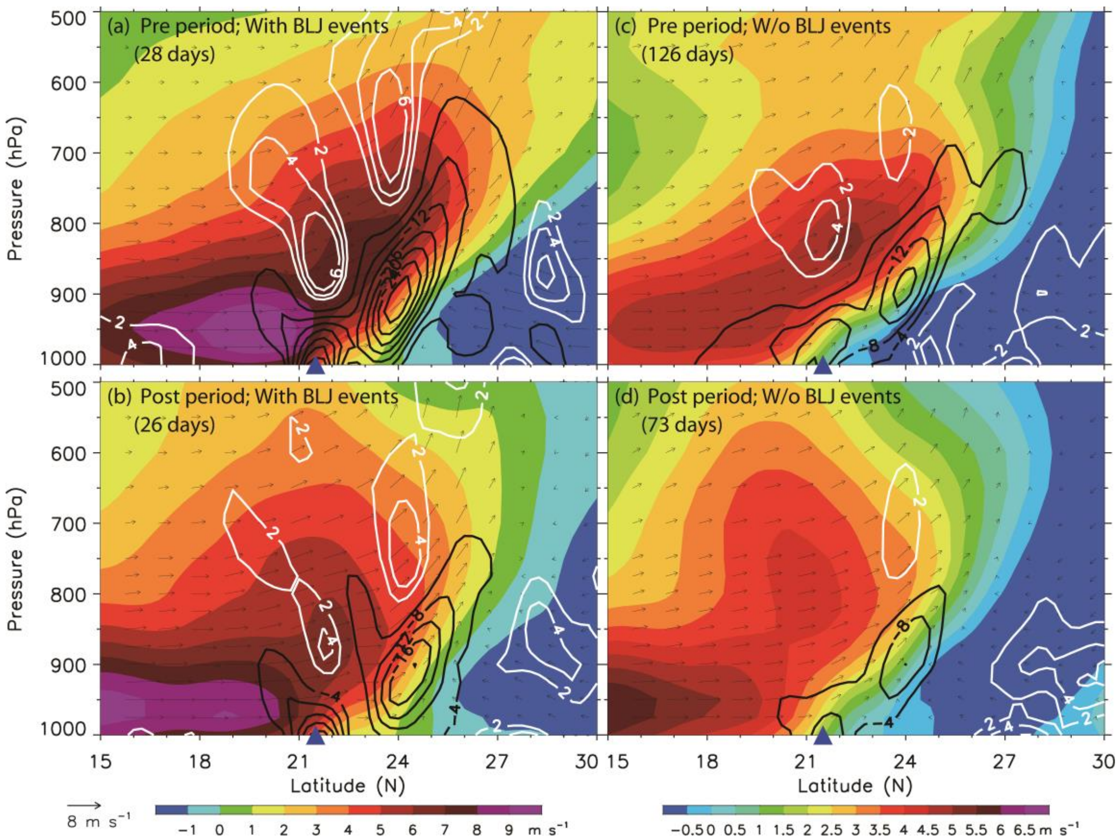


Fig. 13 Vertical cross sections of meridional wind speed (shading), in-plain flow vectors (black vectors; the vertical velocity is multiplied by 200), convergence (black solid; contoured at intervals of $-4\times10^{-6}$ $s^{-1}$) and divergence (white solid; contoured at intervals of $2\times10^{-6}$ $s^{-1}$) along the brown line in Fig. 10b. The variables are averaged for two subgroups of the long-duration rainy days over both the coastal and east-inland regions, i.e., (a-b) with and (c-d) without the BLJ events, respectively. (a) and (c) show the results during the pre-monsoon-onset period and (b) and (d) the post-monsoon-onset period. Blue triangle indicates location of the coastline.

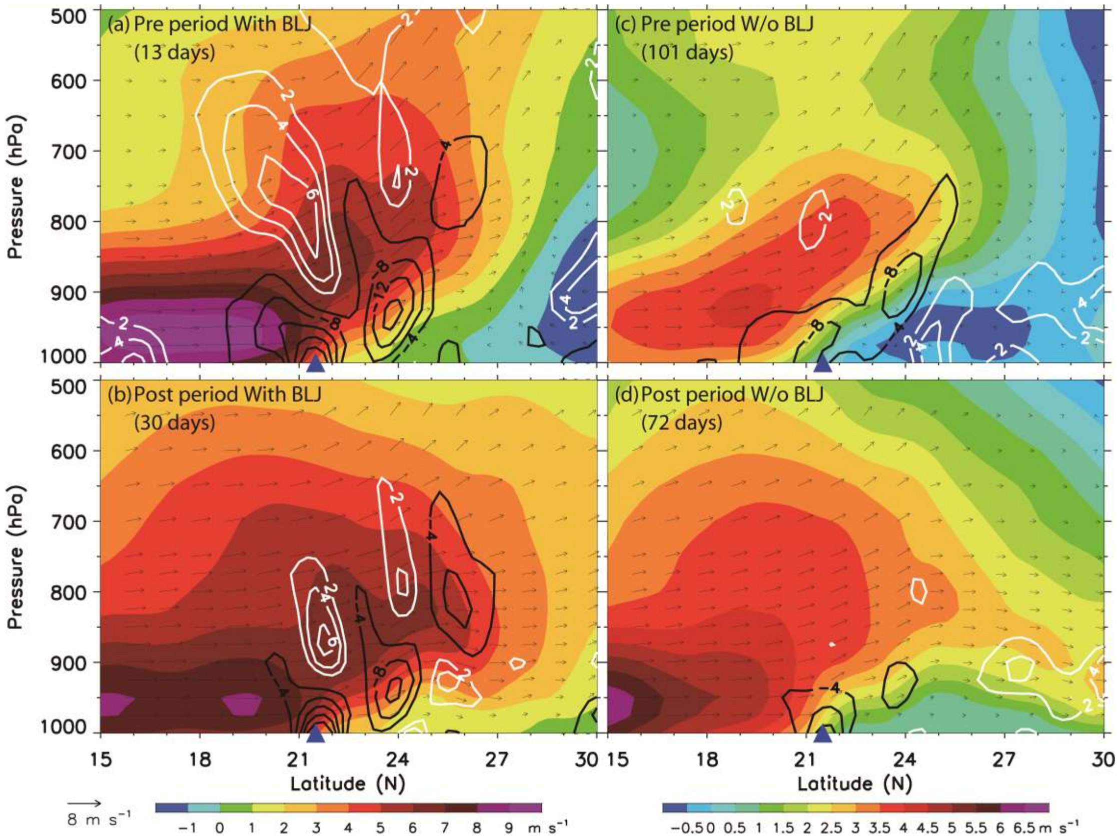


Fig. 14 As in Fig. 13, but for the long-duration rainy days over the coastal region only.